JACS
JOURNAL OF THE AMERICAN CHEMICAL SOCIETY
pubs.acs.org/JACS
Article

Tailorable Indirect to Direct Band-Gap Double Perovskites with Bright White-Light Emission: Decoding Chemical Structure Using Solid-State NMR

Abhoy Karmakar, Guy M. Bernard, Alkiviathes Meldrum, Anton O. Oliynyk, and Vladimir K. Michaelis*

Cite This: J. Am. Chem. Soc. 2020, 142, 10780−10793
Read Online

ABSTRACT: Efficient white-light-emitting single-material sources are ideal for sustainable lighting applications. Though layered hybrid lead−halide perovskite materials have demonstrated attractive broad-band white-light emission properties, they pose a serious long-term environmental and health risk as they contain lead (Pb^{2+}) and are readily soluble in water. Recently, lead-free halide double perovskite (HDP) materials with a generic formula $A(I)_2B'(III)B''(I)X_6$ (where A and B are cations and X is a halide ion) have demonstrated white-light emission with improved photoluminescence quantum yields (PLQYs). Here, we present a series of Bi^{3+}/In^{3+} mixed-cationic $Cs_2Bi_{1-x}In_xAgCl_6$ HDP solid solutions that span the indirect to direct band-gap modification which exhibit tailorable optical properties. Density functional theory (DFT) calculations indicate an indirect−direct band-gap crossover composition when $x > 0.50$. These HDP materials emit over the entire visible light spectrum, centered at 600 ± 30 nm with full-width at half maxima of ca. 200 nm upon ultraviolet light excitation and a maximum PLQY of 34 ± 4% for $Cs_2Bi_{0.085}In_{0.915}AgCl_6$. Short-range structural insight for these materials is crucial to unravel the unique atomic-level structural properties which are difficult to distinguish by diffraction-based techniques. Hence, we demonstrate the advantage of using solid-state nuclear magnetic resonance (NMR) spectroscopy to deconvolute the local structural environments of these mixed-cationic HDPs. Using ultrahigh-field (21.14 T) NMR spectroscopy of quadrupolar nuclei (^{115}In, ^{133}Cs, and ^{209}Bi), we show that there is a high degree of atomic-level $B'(III)/B''(I)$ site ordering (i.e., no evidence of antisite defects). Furthermore, a combination of XRD, NMR, and DFT calculations was used to unravel the complete atomic-level random Bi^{3+}/In^{3+} cationic mixing in $Cs_2Bi_{1-x}In_xAgCl_6$ HDPs. Briefly, this work provides an advance in understanding the photophysical properties that correlate long- to short-range structural elucidation of these newly developed solid-state white-light emitting HDP materials.

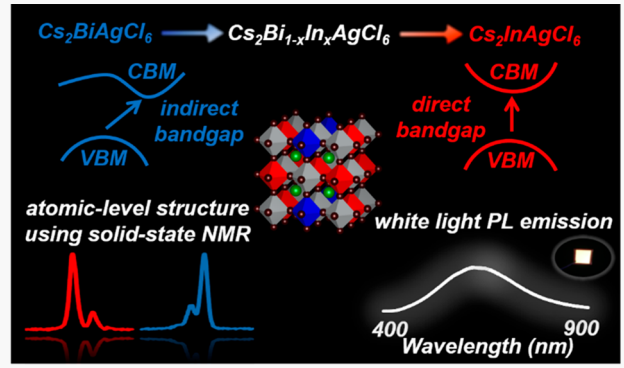

INTRODUCTION

Lead halide perovskite (LHP) materials, with a generic formula ABX_3 (where A = Cs^+, $CH_3NH_3^+$, $CH(NH_2)_2^+$; B = Pb^{2+}; X = Cl^-, Br^-, and I^-) have emerged as a potential disruptive technology due to their remarkable photoconversion efficiencies of 25.2% (single-junction) or 28% when combined with silicon tandem solar cells.[1] Beyond their exciting photovoltaic properties, perovskites have been used in a variety of cost-efficient optoelectronic and electronic applications including light-emitting devices, photodetectors, lasers, water splitting, and X-ray imaging.[2−7] Lighting consumes approximately 20% of the electricity produced globally with growing demand from both developed and developing countries. Identifying sustainable energy solutions, such as highly efficient and low-cost materials for light-emitting diode (LED) applications, is essential. For example, LEDs are expected to produce energy savings of billions of dollars annually in the United States alone.[8]

Recently, halide perovskites have emerged as an attractive light-emitting material due to their near unity photoluminescent quantum yield (PLQY), widely tailorable narrow-band visible-light emission, and cost-efficient solution processability.[2,4,9] Building beyond their photoluminescent properties, structural modifications in LHPs to form two-dimensional (2D) LHPs has yielded materials that show broad-band emission in the visible-light range. For example, the intrinsic broad-band white-light emission which is observed upon ultraviolet excitation is attributed to self-trapped excitons in these 2D LHP materials.[10−12] One such attractive broad-

Received: February 24, 2020
Published: May 19, 2020

https://dx.doi.org/10.1021/jacs.0c02198
J. Am. Chem. Soc. 2020, 142, 10780−10793

band white-light emitting 2D LHP material is (EDBE)$PbBr_4$ (EDBE = 2,2′-(ethylenedioxy)bis(ethylammonium)) with a PLQY of 9%.[12] White-light emission from a single-material source is an attractive avenue for lighting and display applications, since a single-source emitter simplifies device structure and fabrication, avoiding color instability due to the different degradation rates and self-absorption issues encountered with mixed and multiple emitters.[13,14]

Though LHPs have excellent potential for optoelectronic and photovoltaic applications, they suffer from commercialization concerns due to their poor chemical stability[15,16] and have long-term environmental and societal concerns associated with prolonged use of Pb-containing materials.[17,18] For example, bulk LHP materials as well as thin films or LHP solar-cell devices have been shown to undergo chemical decomposition while exposed to ambient light, humid environments, or elevated temperatures.[16,19,20] Moreover, these lead salts are highly soluble in water, which over time has lasting environmental and toxicological implications.[21,22] One avenue being explored to circumvent the lead toxicity of LHPs involves partial (or full) substitution of isoelectronic and low-toxicity elements (i.e., Sn^{2+}, Ge^{2+}) into these materials. Unfortunately, tin(II) and germanium(II) halide perovskite materials are prone to oxidation, creating additional challenges associated with their long-term chemical stability.[23]

As a result of the vast structural and elemental diversity present in the perovskite family, a series of lead-free, chemically stable halide double perovskite (HDP) materials are now being explored as sustainable alternatives to LHPs due to their attractive optical properties both in bulk and in nanocrystals (NCs).[24−34] The general formula of a HDP is $A_2B'(III)B''(I)X_6$, where A is a monovalent cation, B′(III) and B″(I) are trivalent and monovalent cations, respectively, and X is a halide anion. A further benefit of HDP materials compared to LHPs is that they exhibit much higher thermal and moisture resistance.[35−38]

The vast majority of HDPs reported are chloride based with wide band gaps ranging above 2 eV, limiting their ability as solar-absorbing materials. However, these materials have exhibited good photoluminescent (PL) properties with promising quantum yields.[24,32] For example, PL properties for HDPs can be achieved either in the presence of an activator (such as Mn^{2+})[25,27,29,31,39,40] or by a chemical modification on the B′(III) and/or B″(I) site(s).[24,30,41] Orange-light emission of Mn^{2+}-doped $Cs_2InAgCl_6$ NCs has been demonstrated with PLQYs enhanced by an order of magnitude (i.e., ca. 1.6−16%) upon Mn^{2+} doping in $Cs_2InAgCl_6$ NCs.[29] Bi-doped $Cs_2InAg_xNa_{1-x}Cl_6$ HDP provided stable (>1000 h) warm white-light emission with a maximum PLQY of 86%,[24] whereas Bi-doped $Cs_2InAg_xNa_{1-x}Cl_6$ NC was found to have a maximum PLQY of ca. 22%.[42] A broad orange-light emission has been reported from Bi-doped $Cs_2InAgCl_6$ NCs with a PLQY of 11.4%.[34]

Altering the magnitude of the band gap for perovskite materials upon metal alloying is one attractive avenue often reported in the literature.[43−46] Converting materials from an indirect to a direct band-gap semiconductor is less common in semiconducting materials,[47−49] although this offers one stream that could further enable fine tailoring of their optical properties. As most reported HDP materials are either indirect or direct band-gap semiconductors, this class of compounds can support this type of band-gap transformation. For instance, $Cs_2BiAgCl_6$ HDPs exhibit an indirect band gap due to the presence of a lone pair on Bi^{3+} ($6s^2$).[36,50] In contrast, $Cs_2InAgCl_6$ HDPs are direct band-gap semiconductors due to the absence of a lone pair on In(III).[51]

To date, diffraction-based techniques have been used extensively to evaluate the structural properties of HDP materials. These techniques provide long-range structural information but are devoid of detail pertaining to atomic-level structural properties. As a result, atomic-level structural insight of these currently developing HDP materials are not well discussed in the literature. It is essential to characterize the long-range crystalline nature of these materials as well as the complex evolution of short-range structure as Bi^{3+}/In^{3+} cations are mixed in $Cs_2Bi_{1-x}In_xAgCl_6$ HDPs. Solid-state nuclear magnetic resonance (NMR) spectroscopy is one of the most powerful, nondestructive analytical methods able to decode this complex structural evolution and provide insights for the dynamics of these perovskite-based materials.[16,52−72]

These observations motivated us to prepare a series of bulk $Cs_2Bi_{1-x}In_xAgCl_6$ HDP solid solutions where changes in Bi^{3+}/In^{3+} cationic ratios can be associated with an indirect (Bi rich) to direct (In rich) band gap. This collection of HDPs demonstrates how tunable white-light PLQY behavior can be attained. We investigate the unique electronic structures from a first-principles point of view and the photophysical properties using UV−vis and PL techniques for these HDP semiconductors. We further explore the interplay of these materials using robust NMR and XRD measurements as well as density functional theory (DFT) calculations to reveal atomic-level chemical structural insights into the seemingly random Bi^{3+}/In^{3+} cationic mixing (i.e., solid solution in $Cs_2Bi_{1-x}In_xAgCl_6$ HDP materials along with a high degree of B′(III)/B″(I) site ordering). Moreover, antisite defects (i.e., the disorder on B′(III) and B″(I) sites which have similar octahedral environments)[73] and phase segregation upon Bi^{3+}/In^{3+} mixing are also investigated for the complete HDP series.

RESULTS AND DISCUSSION

B′-Site Selection Using Goldschmidt Tolerance Factor Directing Bi/In B′(III)-Site Exchange. A semi-empirical geometric parameter known as the Goldschmidt tolerance factor (t) is often applied to elucidate the structural stability of ABX_3 perovskite materials. It is defined as

$$t = \frac{(r_A + r_X)}{\sqrt{2}(r_B + r_X)} \quad (1)$$

where r_A, r_B, and r_X are the ionic radii of the A, B, and X sites, respectively.[74] Stable perovskite systems are typically formed with 3D octahedral connectivity when t = 0.75−1.00.[75] Another semiempirical geometric parameter is used to define the octahedral stability, known as the octahedral factor (μ), defined as

$$\mu = \frac{r_B}{r_X} \quad (2)$$

Usually BX_6 octahedra are stable when $0.442 \leq \mu \leq 0.895$.[2] The combination of t and μ provides insight into the probability of the formation of a stable perovskite phase. As double perovskites have two different B sites (B′ and B″) and thus r_B is taken as an arithmetic mean of B′ and B″ radii ($r_{B'}$, $r_{B''}$), one can increase the elemental dimensionality (i.e., cation and valency options increase). Applying Shannon's ionic radii,[76] one can obtain (t, μ) values for $Cs_2InAgCl_6$ and

https://dx.doi.org/10.1021/jacs.0c02198
J. Am. Chem. Soc. 2020, 142, 10780−10793

$Cs_2BiAgCl_6$ of (0.937, 0.539) and (0.900, 0.602), respectively. For mixed Bi/In cationic $Cs_2Bi_{1-x}In_xAgCl_6$ solid solutions, t and μ values span between $0.900 \leq t \leq 0.937$ and $0.539 \leq \mu \leq 0.602$, respectively, suggesting that it is possible to form the desired stable perovskite phase for $Cs_2Bi_{1-x}In_xAgCl_6$ ($0 \leq x \leq 1$) solid solutions (Scheme 1).

Scheme 1. Schematic Presentation of the Crystal Structures of the $Cs_2InAgCl_6$ and $Cs_2BiAgCl_6$ Parent Materials and of Their $Cs_2Bi_{1-x}In_xAgCl_6$ Mixed Bi/In Cationic Analogues

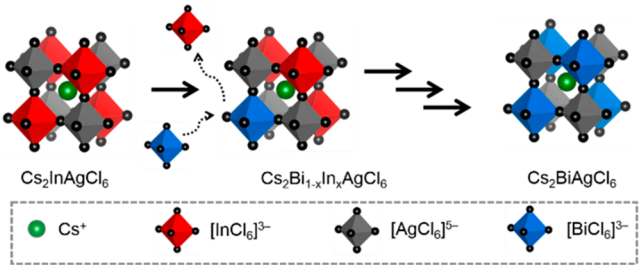

Elemental Composition, Morphology, and Thermal Stability. The $Cs_2BiAgCl_6$ and $Cs_2InAgCl_6$ parent HDPs were synthesized via a solvent-phase synthesis approach starting from their chloride salts, namely, CsCl, $BiCl_3$, $InCl_3$, and AgCl, in concentrated hydrochloric acid media. The mixed Bi^{3+}/In^{3+} cationic analogues, i.e., $Cs_2Bi_{1-x}In_xAgCl_6$ (nominal; x = 0 to 1, Table S1), were synthesized similarly using stoichiometric $BiCl_3$:$InCl_3$ nominal molar ratios. Further synthesis details are discussed in the Supporting Information. Figure 1a illustrates photographs of $Cs_2Bi_{1-x}In_xAgCl_6$ HDPs. The solvent synthesis approach leads to multifaceted micrometer-sized crystals confirmed through field-emission scanning electron microscopy (FESEM) as shown in Figures 1b and S1. Elemental analysis by energy-dispersive X-ray spectroscopy (EDS) indicates that the molar ratio Cs^+:B'^{3+}:Ag^+:Cl^-, where B′ = In, Bi, or both, ≃2:1:1:6 (Table S1), which is the desired elemental composition for the HDP materials. Elemental mapping using EDS analysis shows a homogeneous distribution of all elements (Cs, Bi, In, Ag, and Cl) throughout the powdered solids (Figures 1b and S2). The accuracy of the Bi^{3+}:In^{3+} compositional ratios in the final products were further confirmed using the inductively coupled plasma optical emission spectrometry (ICP-OES) technique (Table S1), which yielded results similar to the nominal Bi^{3+}:In^{3+} batch compositional ratios (Table S2).

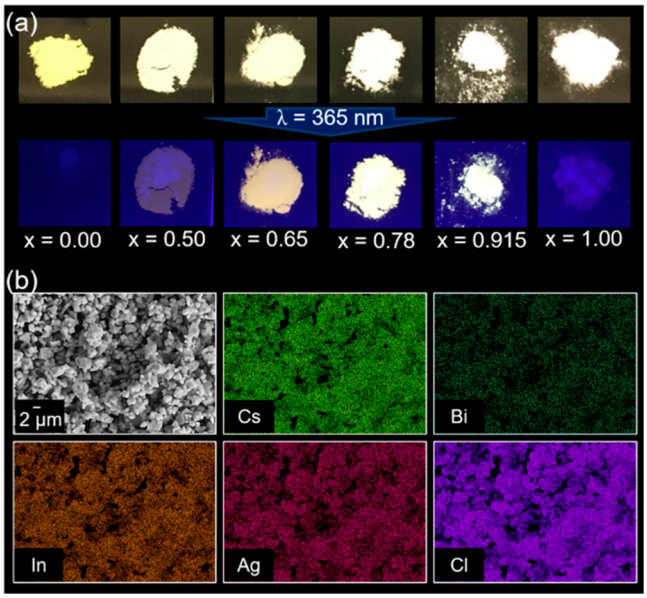

Figure 1. (a) Photographs of $Cs_2Bi_{1-x}In_xAgCl_6$ HDPs under visible (upper row) and UV (lower row, λ = 365 nm) light. (b) FESEM image (2 μm scale) with corresponding EDS elemental mapping showing a homogeneous distribution of Cs (light green), Bi (dark green), In (orange), Ag (pink), and Cl (violet) for $Cs_2Bi_{0.085}In_{0.915}AgCl_6$ HDP polycrystals.

Thermal stability measurements using thermogravimetric analysis (TGA) for $Cs_2BiAgCl_6$ and $Cs_2InAgCl_6$ parents and for one Bi^{3+}/In^{3+} mixed-cationic material, specifically $Cs_2Bi_{0.085}In_{0.915}AgCl_6$, are shown in Figure S3. TGA data indicate that the materials are all thermally stable up to 500 °C and that Bi^{3+}/In^{3+} cationic mixing has a negligible effect on the thermal stability.

Optical and Electronic Band-Gap Tailoring. The optical band-gap properties of $Cs_2Bi_{1-x}In_xAgCl_6$ HDPs were measured by UV−vis diffuse reflectance (DR) spectroscopy. Figure 2a shows the absorbance spectra for the $Cs_2Bi_{1-x}In_xAgCl_6$ HDPs. These absorbance data were obtained from DR measurements and analyzed using the Kubelka−Munk transformation method[77] (see Materials and Methods in the Supporting Information). The experimentally obtained indirect and direct band gaps for the $Cs_2Bi_{1-x}In_xAgCl_6$ HDPs are shown in Figure 2b. $Cs_2BiAgCl_6$ is reminiscent of an indirect band-gap semiconductor due to the mixing between frontier orbitals of Bi and Ag in the valence and conduction band extrema. This has been identified as the origin of the indirect band gaps of Bi−Ag-based HDPs in past studies.[36,78] As substitution of Bi^{3+} with In^{3+} proceeds in a migratory fashion to form $Cs_2InAgCl_6$, a direct band-gap material emerges, where valence-band maxima and conduction band minima originate from In-4d/Ag-4d and In-5s/Ag-5s states, respectively.[51] On the basis of Tauc plots, $(\alpha h\nu)^{1/2}$ vs energy, $Cs_2BiAgCl_6$ exhibits an indirect band gap of 2.70 eV (Figure 2b), agreeing well with an earlier calculated band gap of 2.62 eV using a hybrid functional.[36] A Tauc plot of $(\alpha h\nu)^2$ vs energy indicates that $Cs_2InAgCl_6$ has an experimental direct band gap of 3.67 eV ($\Delta E_g \approx 1$ eV). However, the experimental band gap of $Cs_2InAgCl_6$ is much higher than the calculated fundamental band gap of 2.5 eV because the associated direct band transition is parity forbidden.[79]

This unique behavior for HDP materials, whereby they are either indirect or parity-forbidden direct band-gap materials, leads to inferior absorption behavior around the band gap, rendering them unfavorable candidates for optoelectronic applications such as LEDs.[37,79] These observations motivated us to investigate the optical properties of bulk polycrystalline mixed Bi^{3+}/In^{3+} $Cs_2Bi_{1-x}In_xAgCl_6$ double perovskites. A band structure calculation using DFT with the Heyd−Scuseria−Ernzerhof (HSE06) functional shows that $Cs_2Bi_{1-x}In_xAgCl_6$ materials with $x \leq 0.50$ have an indirect band gap, whereas materials with $x > 0.50$ possess a direct band gap (vide infra). The indirect band gap for $Cs_2Bi_{1-x}In_xAgCl_6$ increases linearly from 2.70 to 2.82 eV as x increases from 0 to 0.50. In contrast, the direct band gap increases from 2.93 to 3.67 eV in an exponential-like fashion for x values ranging from 0.65 to 1 (Figure 2c). The change in the band gap of $Cs_2Bi_{1-x}In_xAgCl_6$ agrees well with the visual color of these materials (Figure 1a); for example, $Cs_2BiAgCl_6$ (x = 0) is pale yellow (2.70 eV), but

https://dx.doi.org/10.1021/jacs.0c02198
J. Am. Chem. Soc. 2020, 142, 10780−10793

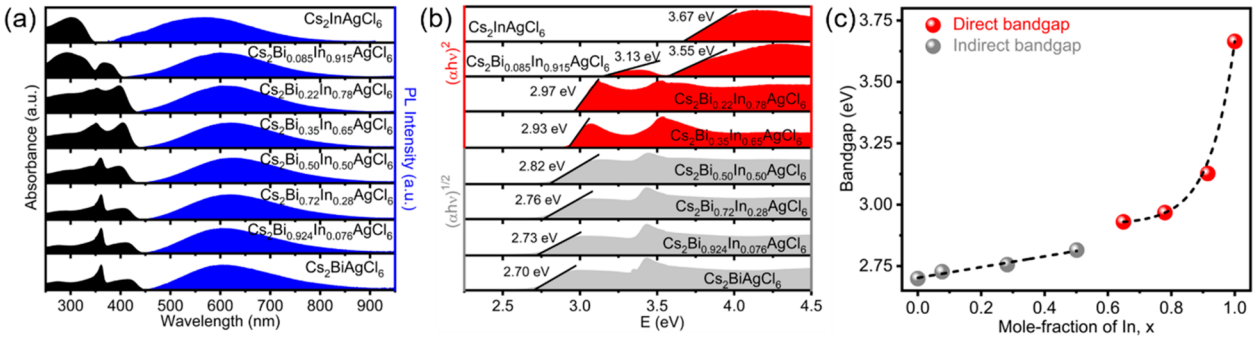

Figure 2. UV−vis absorption spectra (black) and PL spectra (blue) (a), Tauc plots showing indirect ($x \leq 0.5$, gray) and direct ($x > 0.50$, red) band gaps (b) and change in band gap vs indium mole fraction (c) for $Cs_2Bi_{1-x}In_xAgCl_6$ ($0 \leq x \leq 1$) HDPs.

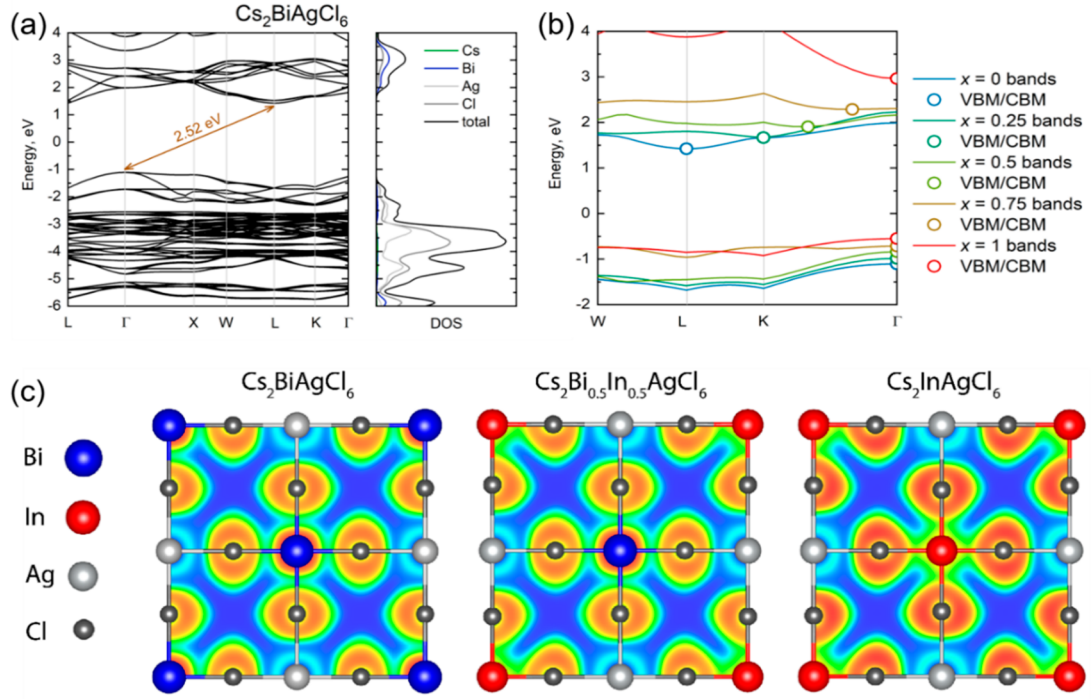

Figure 3. HSE06 DFT band structure and density of states for $Cs_2BiAgCl_6$ (a). Indirect to direct band gap transition in the $Cs_2Bi_{1-x}In_xAgCl_6$ compounds (b). Electron localization function of the $Cs_2Bi_{1-x}In_xAgCl_6$ compounds (c). In c, the 100th slice is shown, with Bi, In, Ag, and Cl atoms located on the plane. Blue, low electron density; red, high electron density.

Table 1. Calculated and Experimental Band Gap Values for $Cs_2Bi_{1-x}In_xAgCl_6$

x	0	0.25	0.5	0.75	1
CBM, eV	1.42 (L)	1.67 (K)	1.91	2.29	2.96 (Γ)
VBM, eV	−1.10 (Γ)	−0.98 (Γ)	−0.83 (Γ)	−0.72 (Γ)	−0.55 (Γ)
HSE06 gap, eV	2.52	2.65	2.74	3.01	3.51
experimental gap, eV	2.70	2.76[a]	2.82	2.97[b]	3.67

[a]The ICP-OES-detected composition is $x = 0.28$. [b]The ICP-OES-detected composition is $x = 0.78$.

as In^{3+} is incorporated, the material becomes increasingly white, with $Cs_2InAgCl_6$ (3.67 eV) appearing as a microcrystalline pristine white solid.

Indirect to Direct Band-Gap Transition Using the Calculated Electronic Band Structure. A transition from an indirect to a direct band gap occurs with Bi to In substitution in the $Cs_2Bi_{1-x}In_xAgCl_6$ ($0 \leq x \leq 1$) HDP series. This case is similar to previously reported isoelectronic Sb to In substitution in $Cs_2Sb_{1-x}In_xAgCl_6$ compounds.[50] The HSE06 DFT functional was applied to correct for the underestimated PBE band gap (Figure 3a), which resulted in good agreement with the band-gap estimation (i.e., 2.52 (DFT) vs 2.70 eV (expt.)). Similar HSE06 DFT band gap and density of states (DOS) plots are available for the rest of the $Cs_2Bi_{1-x}In_xAgCl_6$ series (x = 0.25, 0.5, 0.75, and 1) in the Supporting Information (Figures S4−S7).

The transition from an indirect to a direct band gap was observed in the $Cs_2Bi_{1-x}In_xAgCl_6$ ($0 \leq x \leq 1$) HDP series (Figure 3b). The valence band maximum (VBM) is indicated (Figure 3b), and for each sample it is located at the Γ point.

https://dx.doi.org/10.1021/jacs.0c02198
J. Am. Chem. Soc. 2020, 142, 10780−10793

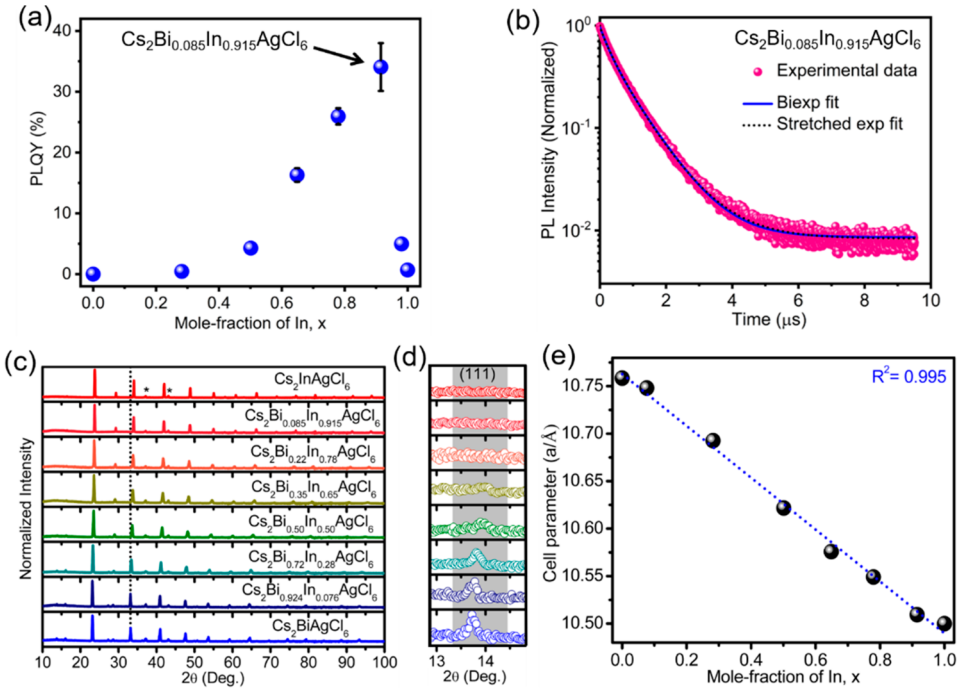

Figure 4. PLQY as a function of indium mole fraction (x) for $Cs_2Bi_{1-x}In_xAgCl_6$ HDPs (a). PL decay for $Cs_2Bi_{0.085}In_{0.915}AgCl_6$ with λ_{ex} = 364 nm and λ_{em} = 625 nm (b). PXRD patterns (c), expansion of the (111) peaks in the PXRD patterns (d), and change in unit cell parameters (e) with indium mole fraction for $Cs_2Bi_{1-x}In_xAgCl_6$ HDPs. In c, dotted line is a guide for the eye and asterisks (*) denote the positions of background signals for all $Cs_2Bi_{1-x}In_xAgCl_6$ HDPs (Figure S16).

The conduction band maximum (CBM), also indicated in Figure 3b, is different for each sample. For $Cs_2BiAgCl_6$, the CBM is at the L symmetry point, composing an indirect Γ−L band gap. With 25% substitution of Bi with In atoms, the band gap still remains indirect (Γ−K). The rest of the solid solution results indicate that the CBM lies between the K and Γ points: with the sample 50% substituted with In, the CBM is closer to K, while for the 75% Bi-substituted sample, the CBM is closer to the Γ point, and as a result, it is measured as a direct Γ−Γ band gap, in good agreement with the experimental values. The end-point compound, $Cs_2InAgCl_6$, has a direct Γ−Γ band gap, with a HSE06 DFT value of 3.51 eV, which agrees well with the experimental value of 3.67 eV. More information is listed in Table 1.

To further utilize DFT tools, electronic properties were investigated with electron localization function (ELF) and Bader charge analyses. Substitution of Bi for In gradually localizes more electron density on the Cl atoms (more intense red cloud about the Cl, Figure 3c); however, the Bader charge values indicate that there is only a dramatic charge change in the end member of the solid solution series (Table S3, Figure S8). In the systems with Bi/In substitution, Ag atom charge differences are negligible and are essentially close to the average Ag charge, regardless of the second-neighbor atom, but the Cl atoms have a 2−3% charge difference, depending on whether Bi or In atoms are in the coordination environment, with the In atom giving a more negative charge on the bonded Cl atoms.

Crystal orbital overlap population (COOP) analyses were undertaken on Cs−Cl, Ag−Cl, Bi−Cl, and In−Cl bonds (Figures S9−S12). These analyses indicate that mostly bonding states are present, resulting in a positive overall contribution in the bonds, with the overall population scaled to the amount of Bi and In in each individual compound. A strong antibonding character is observed near the Fermi level in the Ag−Cl interaction but with the overall bonding states prevailing. Substitution of Bi with In affects the Ag d-band splitting, which is more pronounced in the Bi-containing analogs, broadening the antibonding contributions.

Steady-State and Time-Resolved PL Spectra. All $Cs_2Bi_{1-x}In_xAgCl_6$ samples exhibit broad PL emission ranging from 400 to 850 nm (Figures 2a and S13a) with a nearly constant spectral width of ∼200 nm full width at half-maximum (fwhm) (Figure S13b). The broad PL spectra at ambient temperatures have been attributed to strong electron−phonon Fröhlich interactions in HDP materials.[80] In addition, the emission and excitation wavelengths do not affect the shape of PL excitation or emission spectra, as shown in Figure S14. This result indicates that the white-light emission originates from recombination of the same excitonic state for these HDPs.

$Cs_2InAgCl_6$ shows a PL maximum at 570 nm (2.18 eV), whereas the PL maximum for $Cs_2BiAgCl_6$ is comparatively red shifted and centered at 605 nm (2.05 eV) (Figure S13). The PL maxima extend to a wavelength of 626 nm (1.98 eV) for $Cs_2Bi_{0.50}In_{0.50}AgCl_6$, which is the reddest PL spectrum among the materials (Figure S13c). As a result, the PL emission for all of the materials appeared to be yellowish/orange in color.

The luminescence of the indirect band-gap perovskite materials ($Cs_2Bi_{1-x}In_xAgCl_6$ with $x \leq 0.50$) appeared visibly dim under a UV light, while the perovskites with direct band gaps ($Cs_2Bi_{1-x}In_xAgCl_6$ with $x > 0.50$) revealed bright PL (Figure 1a). $Cs_2InAgCl_6$ in particular did not fit this general trend, however, as it has a direct band gap but displayed faint emission due to the parity-forbidden band transition at the fundamental band gap. The PLQY for $Cs_2Bi_{1-x}In_xAgCl_6$ increased gradually as a function of In concentration, reaching a maximum when x = 0.915 (PLQY = 34 ± 4%); this is

https://dx.doi.org/10.1021/jacs.0c02198
J. Am. Chem. Soc. 2020, 142, 10780−10793

followed by a stark decrease in PLQY upon reaching the pure endmember $Cs_2InAgCl_6$, Figure 4a. Although $Cs_2InAgCl_6$ exhibits a direct band gap, it too suffers from a low PLQY (<1%) due to the In-5s orbital beginning to dominate in the conduction band, which is in good agreement with DFT calculations (Figures S4−S7).[79] As a result, the parity-forbidden transition from the valence band to the conduction band becomes quite long and is no longer competitive with the nonradiative (faster) recombination causing a lower PLQY.

The time-resolved PL spectrum for $Cs_2Bi_{0.085}In_{0.915}AgCl_6$ (with maximum PLQY) is shown in Figure 4b. Several decay models were fit using a nonlinear least-squares fitting algorithm, including a single exponential, a biexponential, and a stretched exponential (Figure S15). While the correct model is difficult to determine unambiguously from these data, the biexponential and stretched exponential gave the lowest sum of squares of the residuals and showed comparatively little bias in the residuals, Table S4. The biexponential model results yielded a fast component with a time constant of 279 ns (36%) and a slow component of 865 ns (64%). From these two components, a weighted mean time constant of 774 ns can be extracted for comparative purposes. The stretched exponential yielded similar although slightly longer mean time constants calculated according to $\tau = \tau_{SE}[\Gamma(2/\beta)/\Gamma(1/\beta)]$,[81] where τ_{SE} is the time constant obtained from the stretched exponential model fit and β is the stretching parameter. A comparable behavior is observed for $Cs_2Bi_{0.22}In_{0.78}AgCl_6$, which gave a weighted mean biexponential lifetime of 978 ns. The PL decay traces and average lifetimes were nearly the same upon changing the wavelength from 550 to 700 nm (using a monochromator with an 8 nm band pass) for both materials (Figure S15 and Table S5). This result suggests that the broad-band emission is unlikely to arise from different mechanisms in these HDP materials. A similar observation has been noted in 2D LHP material.[82] In contrast, $Cs_2InAgCl_6$ shows two different transition mechanisms with short (<10 ns) and long (tens to hundreds of nanoseconds) PL lifetime components, where the longer lifetime component is attributed to the parity-forbidden transitions from CBM to VBM.[83] We further note that the PL lifetime of $Cs_2InAgCl_6$ HDP is insensitive to the intensity of the pump laser,[51] whereas different excitation flux may explain some of the differences in the reported dynamics in LHP materials.[84,85]

Insight into HDP Chemical Structure from XRD and NMR Spectroscopy. The $Cs_2BiAgCl_6$ and $Cs_2InAgCl_6$ parent materials are phase pure and adopt a face-centered cubic double perovskite lattice (space group $Fm\bar{3}m$) with unit cell constants of 10.7584(14) and 10.5000(12) Å, respectively. The small difference (<3%) in the unit cell parameters between $Cs_2BiAgCl_6$ and $Cs_2InAgCl_6$ allows formation of mixed-cationic, $Cs_2Bi_{1-x}In_xAgCl_6$ HDP solid solutions that adopt the same $Fm\bar{3}m$ space group. Since the ionic radii of In^{3+} ($r(In^{3+})$ = 80 pm) are less than those of Bi^{3+} ($r(Bi^{3+})$ = 103 pm),[76] the diffraction peak is sequentially shifted to a higher 2θ value with increasing In^{3+} content in $Cs_2Bi_{1-x}In_xAgCl_6$ (Figure 4c) as the unit cell decreases in volume. It has been shown that the appearance of a (111) diffraction peak is fundamentally related to the B′(III) and B″(I) site ordering in $Cs_2InAg_xNa_{1-x}Cl_6$ HDPs.[24] The appearance of (111) diffraction peaks in $Cs_2Bi_{1-x}In_xAgCl_6$ HDPs also indicates a high degree B′(Bi^{3+}, In^{3+}) and B″(Ag^+) site ordering (Figure 4d).

The presence of an intense (111) diffraction peak for the $Cs_2BiAgCl_6$ parent indicates extremely well-ordered Bi^{3+} and Ag^+ cationic sites, further supported by the NMR, vide infra. The peak intensity decreases with increasing In^{3+} concentration (i.e., $Cs_2Bi_{1-x}In_xAgCl_6$ HDPs) and becomes undetectable for the $Cs_2InAgCl_6$ parent material. The isoelectronic nature of In^{3+} and Ag^+ cations limits the sensitivity of the (111) diffraction peak, and it becomes uninformative for B′(III) and B″(I) site cation ordering for the $Cs_2InAgCl_6$ parent and In^{3+}-rich $Cs_2Bi_{1-x}In_xAgCl_6$ HDP materials. We therefore applied NMR spectroscopy to understand the atomic-level ordering of these materials. The cell parameters for the mixed-cation $Cs_2Bi_{1-x}In_xAgCl_6$ compounds extracted from the PXRD patterns show a linear relationship as a function of In concentration as shown in Figure 4e. This result is consistent with Vegard's law,[86] whereby the mixed B′(III) site HDP, $Cs_2Bi_{1-x}In_xAgCl_6$, demonstrates solid solution behavior.

Diffraction approaches provide insight into the long-range structure of these $Cs_2Bi_{1-x}In_xAgCl_6$ perovskite materials. Most of the HDP parent materials rely on structural elucidation using these techniques. However, it has been shown that solid-state NMR spectroscopy yields a deeper understanding of local (<5 Å)- and medium (5−10 Å)-range structure when cation and anion doping (or mixing) is present in perovskite-based materials.[52,53,63,66−72] Previously, we used ^{133}Cs and ^{121}Sb NMR spectroscopy to unravel unique structural motifs for paramagnetic Cu(II)-doped $Cs_2SbAgCl_6$ HDPs.[70] Here, we performed ^{115}In, ^{133}Cs, and ^{209}Bi NMR spectroscopy to improve our structural understanding of the A(^{133}Cs) and B′(^{209}Bi and ^{115}In) sites for $Cs_2Bi_{1-x}In_xAgCl_6$ solid solutions.

Cesium-133 NMR Spectroscopy of the A Site. The cesium ion in $Cs_2InAgCl_6$ or $Cs_2BiAgCl_6$ resides in a cuboctahedral void surrounded by either four $[InCl_6]^{3-}$ or four $[BiCl_6]^{3-}$ octahedra alternating with four $[AgCl_6]^{5-}$ octahedra, as shown in Scheme 1. Their proximity to B′(III) sites of the $Cs_2Bi_{1-x}In_xAgCl_6$ materials makes ^{133}Cs an ideal NMR nucleus to study changes occurring in the crystalline system. Quadrupolar ^{133}Cs (nuclear spin, I = 7/2, Q_m = −0.34 fm^2, 100% natural abundance) is a highly sensitive NMR nucleus with excellent resolution, as it behaves as a pseudo-spin-1/2 nucleus, rendering it ideal to investigate small changes in its local coordination environment.[87−90] Crystallographically, there is only one cesium site in the parent materials, $Cs_2InAgCl_6$ and $Cs_2BiAgCl_6$, giving sharp peaks (fwhm = 1 ppm) with distinguishable ^{133}Cs NMR isotropic chemical shifts, $\delta_{iso}(^{133}Cs)$, of 122(1) and 77(1) ppm, respectively (Figure 5). The parent phases are highly symmetric with a high degree of B′(III)/B″(I) cation ordering and both B′(III) or B″(I) sites giving tetrahedral symmetry at the Cs site; in other words, cesium cations reside at the center of a perfect cuboctahedra, surrounded by 12 chlorides with equal Cs−Cl distances for the parent materials ($Cs_2BiAgCl_6$ and $Cs_2InAgCl_6$). Hence, the vanishing C_Q suggests a very low level of defects.

To further understand the In^{3+}/Bi^{3+} mixed-cationic $Cs_2Bi_{1-x}In_xAgCl_6$ system, we performed ^{133}Cs MAS NMR spectroscopy on the complete series (Figure S17). Figure 5 shows ^{133}Cs MAS NMR spectra for Bi^{3+}-doped $Cs_2Bi_{0.085}In_{0.915}AgCl_6$ with three resolved ^{133}Cs NMR resonances centered at 121, 115, and 109 ppm and with a ratio of 78:20:2 (fitted peak area; ±2%), which follow a binominal-like distribution (Figure S18 and Supplementary Note 1). This

https://dx.doi.org/10.1021/jacs.0c02198
J. Am. Chem. Soc. 2020, 142, 10780−10793

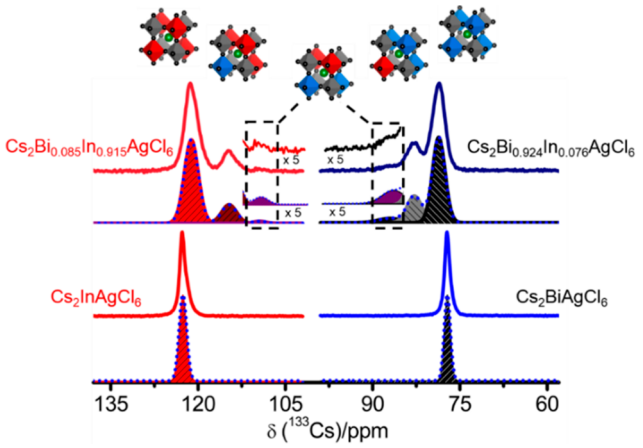

Figure 5. Solid-state ^{133}Cs MAS NMR spectra (solid lines) and its overall best Gaussian fits (blue dotted lines) for $Cs_2BiAgCl_6$ and $Cs_2InAgCl_6$ parents and their In^{3+}- or Bi^{3+}-doped materials, namely, $Cs_2Bi_{0.924}In_{0.076}AgCl_6$ and $Cs_2Bi_{0.085}In_{0.915}AgCl_6$, respectively. Spectra were acquired at a magnetic field strength of 21.14 T with a spinning frequency of 30 kHz. Gray octahedra represent $[AgCl_6]^{5-}$, red octahedra represent $[InCl_6]^{3-}$, and blue octahedra represent $[BiCl_6]^{3-}$.

statistical distribution suggests atomic-level solid solution behavior upon Bi^{3+}/In^{3+} mixing that would be consistent with the associated Vegard's analysis, vide supra. The peak at $\delta_{iso}(^{133}Cs)$ = 121 ppm is assigned to the parent $Cs_2InAgCl_6$, where Cs^+ is surrounded alternatively by four $[InCl_6]^{3-}$ and four $[AgCl_6]^{5-}$ octahedra, whereas the other two peaks to lower frequencies at 115 and 109 ppm correspond to one $[InCl_6]^{3-}$ and two $[InCl_6]^{3-}$ octahedra substituted by one $[BiCl_6]^{3-}$ and two $[BiCl_6]^{3-}$ octahedra, respectively.

Similarly, Figure 5 shows ^{133}Cs NMR spectra for the In^{3+}-doped component, i.e., $Cs_2Bi_{0.924}In_{0.076}AgCl_6$, which show three resolved $\delta_{iso}(^{133}Cs)$ peaks at 79, 83, and 87 ppm with a fitted peak area ratio of 70:25:5 (±2%) that also follow a binomial-like distribution (Figure S18); these peaks are attributed to the bismuth parent ($Cs_2BiAgCl_6$), one and two $[InCl_6]^{3-}$ substitutions at a $[BiCl_6]^{3-}$ site, respectively. Though the local Cs environment for the third low-intensity ^{133}Cs NMR resonances for both $Cs_2Bi_{0.085}In_{0.915}AgCl_6$ (109 ppm) and $Cs_2Bi_{0.924}In_{0.076}AgCl_6$ (87 ppm) are similar (i.e., Cs is surrounded by two $[InCl_6]^{3-}$ and two $[BiCl_6]^{3-}$ octahedra), the chemical shift is significantly different due to the composition and the long-range crystal structure. Beyond dopant quantities (i.e., <10%) of Bi^{3+} or In^{3+}, the ^{133}Cs NMR resonances broaden and shift to lower and higher frequencies between the two parent phases, further limiting resolution. For example, $Cs_2InAgCl_6$ has a $\delta_{iso}(^{133}Cs)$ of 122 ppm and a fwhm of ca. 130 Hz vs $\delta_{iso}(^{133}Cs)$ of 117 ppm and fwhm ca. 650 Hz for $Cs_2Bi_{0.22}In_{0.78}AgCl_6$, although both resonances correspond to Cs^+ surrounded by four $[InCl_6]^{3-}$ and four $[AgCl_6]^{5-}$ (Figure S17b). Gradual changes in isotropic chemical shifts as the unit cell volume changes have previously been observed for NMR spectroscopy of other halide perovskite systems, such as ^{133}Cs (Cu^{2+}-doped $Cs_2SbAgCl_6$) and ^{207}Pb ($APb(Cl/Br)_3$, where A = Cs^+, $CH_3NH_3^+$, or $CH(NH_2)_2^+$.[52,63,66,70] For higher In^{3+}/Bi^{3+} mixed $Cs_2Bi_{1-x}In_xAgCl_6$ materials with $0.10 < x < 0.90$, ^{133}Cs NMR resonances are inhomogeneously broadened due to the possible substitution patterns of Bi and In of the next-nearest neighboring octahedra and beyond, further limiting resolution. The Cs environments span a chemical shift range of 44 ppm, inhibiting baseline resolution and thus limiting our ability to deconvolute the multiple ^{133}Cs NMR sites (Figure S17). Nonetheless, ^{133}Cs NMR chemical shift maxima for $CsIn_{0.50}Bi_{0.50}AgCl_6$, corresponding to two $[InCl_6]^{3-}$ and two $[BiCl_6]^{3-}$ within its cuboctahedron site, is exactly the average of the two parent resonances with $\delta_{max}(^{113}Cs)$ = 99 ppm (Figure S17c).

Bismuth-209 and Indium-115 NMR Spectroscopy of the B′(III) Sites. Both B′(III) site cations, ^{209}Bi (N.A. = 100%) and ^{115}In (N.A. = 95.7%), are quadrupolar nuclei (I = 9/2) with quadrupole moments ($Q_m(^{209}Bi)$ = −51.6 fm^2 and $Q_m(^{115}In)$ = 81 fm^2)) that are more than two orders of magnitude greater than that for ^{133}Cs. These intrinsic NMR properties can potentially lead to significant second-order quadrupolar broadening of the central transition.[87,91−93] Figure 6a shows

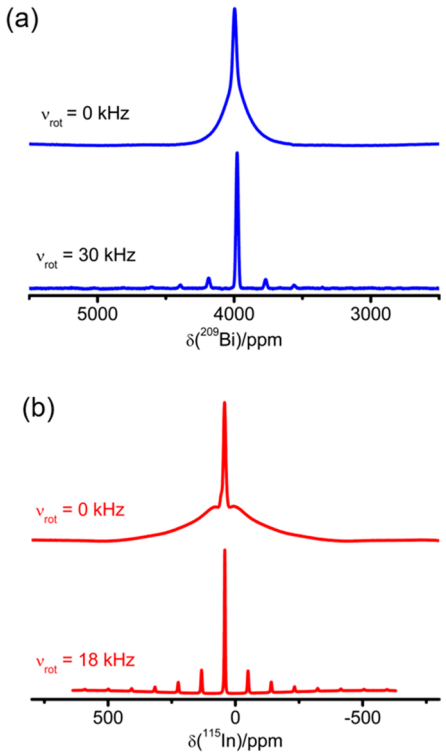

Figure 6. Solid-state ^{209}Bi (a) and ^{115}In (b) NMR spectra for the $Cs_2BiAgCl_6$ and $Cs_2InAgCl_6$ parent materials. NMR spectra were acquired at 21.14 T with and without magic-angle sample spinning as indicated.

the nonspinning ^{209}Bi NMR spectrum for the $Cs_2BiAgCl_6$ parent material acquired at 21.14 T. Bismuth-209 NMR spectroscopy for $Cs_2BiAgCl_6$ gives a sharp resonance at ca. 4000 ppm with no evidence of second-order quadrupolar broadening as expected from its high local octahedral symmetry. A broad underlying component was observed, spanning between ca. 3600 and 4400 ppm, which breaks into a series of first-order spinning side bands upon magic-angle spinning (Figure 6a), corresponding to the satellite transition manifold. Comparing ^{209}Bi NMR spectra at multiple magnetic field strengths, i.e., $\mathbf{B}_0$ = 7.05, 11.75, and 21.14 T (Figure S19), a small ^{209}Bi C_Q of 0.80 ± 0.20 MHz is obtained for $Cs_2BiAgCl_6$, which leads to no significant second-order broadening (ca. 20 Hz) of the central transition, unlike the typically significant second-order quadrupolar broadening (order of MHz) that is observed in cases where there is a

https://dx.doi.org/10.1021/jacs.0c02198
J. Am. Chem. Soc. 2020, 142, 10780−10793

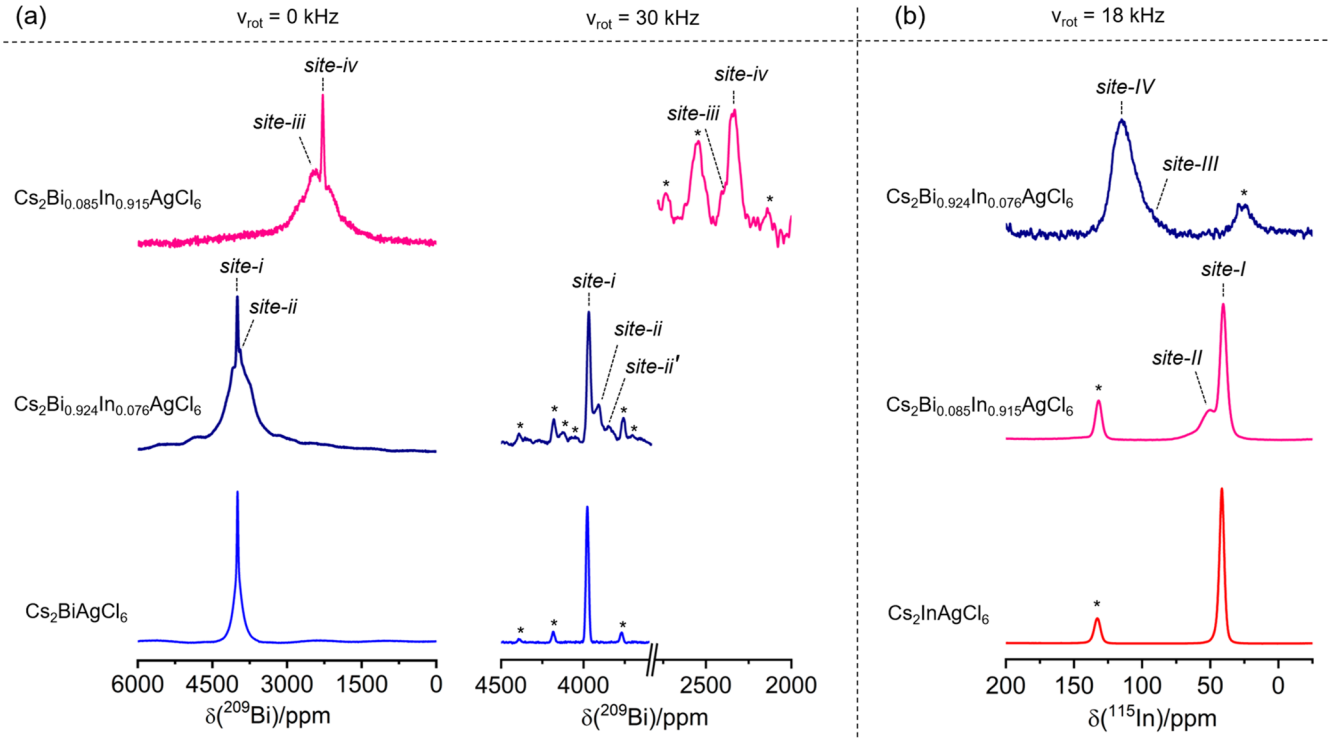

Figure 7. Solid-state ^{209}Bi NMR spectra for the $Cs_2BiAgCl_6$ parent, $Cs_2Bi_{0.924}In_{0.076}AgCl_6$, and $Cs_2Bi_{0.085}In_{0.915}AgCl_6$ materials (a). Solid-state ^{115}In NMR spectra for the $Cs_2InAgCl_6$ parent, $Cs_2Bi_{0.085}In_{0.915}AgCl_6$, and $Cs_2Bi_{0.924}In_{0.076}AgCl_6$ materials (b). Spectra were acquired at 21.14 T with and without magic-angle spinning as indicated. Asterisks (*) indicate spinning side bands.

lower symmetry chemical environment about Bi; for example, $Bi(CH_3CO_2)_3$ results in a very large C_Q of 256 MHz.[93] Therefore, broadening of the central transition peak (fwhm = 2.8 kHz) under MAS conditions is not due to the second-order quadrupolar interaction. This line width is decreased from the 7.5 kHz observed in the absence of spinning, suggesting that heteronuclear dipolar coupling is also a factor but not the sole source of the observed broadening. A previous study on lead halide perovskite systems[67,94] demonstrated that indirect spin−spin (J) coupling between the halide atoms and ^{207}Pb is a significant factor in the observed ^{207}Pb line widths in those systems.[95] Thus, the broadening of the ^{209}Bi central transition is attributed to both direct and indirect spin−spin interactions between ^{209}Bi and the six directly coordinated $^{35/37}$Cl nuclei. The lack of resolution for these fine couplings is attributed to spin−spin (i.e., T_2) relaxation.

The $[BiCl_6]^{3-}$ (or $[InCl_6]^{3-}$) and $[AgCl_6]^{5-}$ octahedra are alternately arranged in the HDP crystal structure to form the $Cs_2BiAgCl_6$ (or $Cs_2InAgCl_6$) parent material. The central Bi atom is surrounded by six $[AgCl_6]^{5-}$ followed by a set of $[BiCl_6]^{3-}$ octahedra, which repeats (i.e., along one dimension the atoms are arranged as follows, Bi−Cl−Ag−Cl−Bi). As such, the central $[BiCl_6]^{3-}$ octahedron is surrounded by a total of 12 $[BiCl_6]^{3-}$ octahedra in the first B′(III) coordination sphere (∼8 Å) within the structure (Figure S20a). As the EFG is sensitive to the minute B′(III) site mixing, as the medium-range symmetry begins to break down, distinct NMR line shapes and breadths for each possible combination can occur. The system becomes increasingly complex once significant Bi/In substitution is considered due to the multiple distinct Bi chemical environments. A second B′(III) coordination sphere (<12 Å) may further exacerbate this, where an additional six sites could also contribute to changes in the EFG for these large quadrupole-moment nuclei (Figure S20b). Therefore, the resulting ^{209}Bi NMR spectra of these materials may appear broad and be spectrally unresolved due to the overlap of multiple chemical shifts and quadrupolar coupling parameters when solid solutions are formed. In light of the complex situation, assigning the source for any impacts at a given NMR site must be tentative. In the ensuing, we assume that a given center is only impacted by substitutions in the first B′(III) coordination sphere, because of the much greater distance of octahedra in the second B′(III) coordination sphere and lower probability of substitution at these sites (6 sites compared to 12 in the first B′(III) coordination sphere), but another possibility is that EFGs resulting from substitutions in the first B′(III) coordination sphere are such that their impact is not detected (vide infra) and that we are in fact detecting the impact from substitutions at the greater distance.

Nevertheless, to extract some further structural insight, a strategic low-doping approach was performed and is shown in Figure 7a (^{209}Bi NMR) and 7b (^{115}In NMR) for $Cs_2Bi_{0.085}In_{0.915}AgCl_6$ and $Cs_2Bi_{0.924}In_{0.076}AgCl_6$. The low In^{3+}-doping concentration in $Cs_2Bi_{0.924}In_{0.076}AgCl_6$ renders statistically improbable multiple substitutions (i.e., substitution of only one $[InCl_6]^{3-}$ octahedron out of 13 $[BiCl_6]^{3-}$ octahedra, $\left(\frac{x(\mathrm{In})}{x(\mathrm{In})+x(\mathrm{Bi})} \approx \frac{1}{13}\right)$). Therefore, the Bi center will recognize one $[InCl_6]^{3-}$ octahedron on average within the medium-range structure. Unfortunately, the substitution during crystal growth will be random across the 12 possible B′(III) positions that are surrounding the Bi center. The same explanation is applicable for the In system ($Cs_2Bi_{0.085}In_{0.915}AgCl_6$) as well. The labels in Figure 7 represent new ^{209}Bi and ^{115}In NMR resonances for a single

https://dx.doi.org/10.1021/jacs.0c02198
J. Am. Chem. Soc. 2020, 142, 10780−10793

or double B′(III) site substitution(s) in our doped HDP system, as discussed below.

Upon doping with In^{3+} to form $Cs_2Bi_{0.924}In_{0.076}AgCl_6$, a second broad low-intensity ^{209}Bi resonance appears to lower frequency (Figure 7a). The high-frequency resonance is assigned to $(BiCl_6)^{3-}$ surrounded by six $\{AgCl_6\}^{5-}$ octahedra and then by 12 $[BiCl_6]^{3-}$ octahedra in the first B′(III) coordination sphere, noted as *site-i* (i.e., $(BiCl_6)\{AgCl_6\}_6[BiCl_6]_{12}$), with a center-of-gravity shift, $\delta_{cgs} \approx 3980$ ppm. The low-intensity resonance to lower frequency with $\delta_{cgs} \approx 3920$ ppm (*site-ii*) is tentatively assigned to ^{209}Bi nuclei where one of the $[BiCl_6]^{3-}$ positions in the first B′(III) coordination sphere has been replaced by a single $[InCl_6]^{3-}$ octahedron (i.e., $(BiCl_6)\{AgCl_6\}_6[BiCl_6]_{11}[InCl_6]_1$).

Likewise, the ^{209}Bi MAS NMR data for the same sample appears to have a low-intensity third resonance at $\delta_{cgs} = \sim 3860$ ppm, which is tentatively assigned as the signal due to sites where two $[BiCl_6]^{3-}$ octahedra in the first B′(III) octahedral coordination environment are replaced by two $[InCl_6]^{3-}$, i.e., *site-ii′*, $(BiCl_6)\{AgCl_6\}_6[BiCl_6]_{10}[InCl_6]_2$ (Figures 7a and S21). A slight broadening of the high-frequency resonance is also observed (ca. 2.8 kHz $Cs_2BiAgCl_6$ vs ca. 3.2 kHz for $Cs_2Bi_{0.924}In_{0.076}AgCl_6$) which is attributed to a reduction in medium-range symmetry about the central $(BiCl_6)^{3-}$ octahedron.

For $Cs_2Bi_{1-x}In_xAgCl_6$ samples with higher indium mole fractions (i.e., $Cs_2In_{0.28}Bi_{0.72}AgCl_6$, $Cs_2In_{0.50}Bi_{0.50}AgCl_6$, $Cs_2In_{0.78}Bi_{0.22}AgCl_6$), multiple resonances are observed to low frequency in the ^{209}Bi NMR spectra compared to that for $Cs_2BiAgCl_6$ (Figure S22). These multiple sites correspond to distinct ^{209}Bi chemical environments which arise from the variation of $[InCl_6]^{3-}$ and $[BiCl_6]^{3-}$ substitutions in the medium-range chemical environment with respect to the central $(BiCl_6)^{3-}$ unit. Interestingly, for the very low bismuth-containing material, $Cs_2Bi_{0.085}In_{0.915}AgCl_6$, two distinguishable ^{209}Bi NMR sites centered at $\delta_{cgs} = \sim 2280$ and $\delta_{cgs} = \sim 2450$ ppm are observed (Figure 7a). The low-frequency Gaussian-like sharp ^{209}Bi peak at 2280 ppm (*site-iv*) corresponds to a very symmetric $(BiCl_6)^{3-}$ octahedral site surrounded by $[InCl_6]^{3-}$ octahedra in the first B′(III) octahedral environment, i.e., $(BiCl_6)\{AgCl_6\}_6[InCl_6]_{12}$. The broad peak at the higher frequency region ($\delta_{cgs} = \sim 2450$ ppm, *site-iii*) corresponds to a $(BiCl_6)\{AgCl_6\}_6[BiCl_6]_1[InCl_6]_{11}$ site. This composition is also where the maximum PLQYs are observed, consistent with the importance of the doping of Bi in $Cs_2InAgCl_6$ as noted above.

Indium-115 NMR spectra were acquired at 21.14 T for the complete series of $Cs_2Bi_{1-x}In_xAgCl_6$ solid solutions. Figure 6b shows the ^{115}In nonspinning and MAS NMR spectra for the $Cs_2InAgCl_6$ parent material. Similar to the ^{209}Bi NMR data discussed above, the ^{115}In NMR spectrum shows a sharp central transition resonance, $\delta_{cgs} = \sim 42$ ppm. The absence of a second-order quadrupolar interaction is due to the octahedral symmetry of the In^{3+} environment formed by six coordinating Cl^-, $(InCl_6)^{3-}$, and by the overall high symmetry of the medium-range structure (i.e., each In octahedron is surrounded by six $\{AgCl_6\}^{5-}$ and 12 $[InCl_6]^{3-}$octahedra in the first B′(III) coordination environment, $(InCl_6)\{AgCl_6\}_6[InCl_6]_{12}$, *site-I*). The line shape is Gaussian-like with the bulk of the broadening attributed to both direct and indirect spin−spin coupling between ^{115}In and six directly attached $^{35/37}$Cl to form $InCl_6^{3-}$ octahedra, as observed for the ^{209}Bi NMR spectrum for $Cs_2BiAgCl_6$. Along with the central transition, a broad underlying component, spanning between ca. 500 and −400 ppm, corresponds to the ^{115}In satellite transitions.[96,97] Using the field dependence of the quadrupole coupling interaction, a small $C_Q(^{115}In)$ of 1.10 ± 0.25 MHz was calculated for $Cs_2InAgCl_6$ (Figure S23). As bismuth is incorporated at low concentrations to form $Cs_2Bi_{0.085}In_{0.915}AgCl_6$, a second broad ^{115}In MAS NMR resonance appears at higher frequency at $\delta_{cgs} = \sim 50$ ppm (*site-II*), along with the sharp resonance observed for the parent material (Figure 7b). The broadening in the new resonance is due to an increase in the EFG about the indium center as one $[InCl_6]^{3-}$ octahedron is replaced by a $[BiCl_6]^{3-}$ octahedron, breaking the medium-range symmetry, i.e., *site-II*, $(InCl_6)\{AgCl_6\}_6[InCl_6]_{11}[BiCl_6]_1$. Likewise, examination of the central transition peaks for the ^{115}In MAS NMR spectra indicates a broadening with the fwhm increasing 160% from ca. 0.7 ($Cs_2InAgCl_6$) to ca. 1.1 kHz ($Cs_2Bi_{0.085}In_{0.915}AgCl_6$), similar to what was discussed above for the ^{209}Bi spectra. Figure S24 shows ^{115}In NMR spectra for the full $Cs_2Bi_{1-x}In_xAgCl_6$ HDP series. As the bismuth mole fraction increases, multiple ^{115}In NMR resonances are observed in the higher frequency region (e.g., $Cs_2Bi_{0.22}In_{0.78}AgCl_6$), along with the central transition peak for the parent compound. However, for samples with much higher bismuth mole fractions, i.e., for $Cs_2Bi_{0.50}In_{0.50}AgCl_6$ and for $Cs_2Bi_{0.72}In_{0.28}AgCl_6$, nearly Gaussian-like ^{115}In NMR line shapes centered between ca. 85 and 105 ppm, respectively, are observed. For materials with low indium, $Cs_2Bi_{0.924}In_{0.076}AgCl_6$, an asymmetric narrow line shape ($\delta_{cgs} = \sim 115$ ppm, *site-IV*) is observed. *Site-IV* corresponds to $(InCl_6)^{3-}$ octahedra surrounded by 12 $[BiCl_6]^{3-}$ octahedra in the first B′(III) octahedral coordination environment (i.e., $(InCl_6)\{AgCl_6\}_6[BiCl_6]_{12}$).

Turning our attention back to the cubic parent compounds, the observation of spinning side bands and nonzero C_Qs for ^{209}Bi and ^{115}In is direct evidence of the presence of defects. The exact concentration of defects cannot be determined precisely; however, some qualitative insight can be gained from examination of the ^{133}Cs, ^{209}Bi, and ^{115}In NMR spectra of the parent compounds. The ^{133}Cs MAS NMR spectra of the parent materials are dominated by a sharp single isotropic resonance with only a single low-intensity (<1%) spinning side band upon slow (5 kHz) magic-angle spinning conditions (Figure S17a). On the basis of past studies, the small spinning side band may be attributed to chloride vacancies (V_{Cl}) as halogen vacancies are one of the dominant and stable point defects in HDP due to their low formation energy.[73,98] It has also been shown to be energetically favored to have alternating $AgCl_6$ and $BiCl_6$ site arrangements for $Cs_2BiAgCl_6$; the electronic configuration of B′(III) site cations plays an important role in the halogen vacancies, where $Cs_2InAgCl_6$ has a lower V_{Cl} formation energy than that for $Cs_2BiAgCl_6$ due to the absence of an s orbital in In^{3+} ion.[99] The ^{133}Cs quadrupole moment is ∼240 times smaller than that for ^{115}In (or ∼150 times smaller than that for ^{209}Bi); therefore these small V_{Cl} defects would manifest more readily as a series of spinning side bands for both ^{115}In and ^{209}Bi spectra, which are shown in Figures S24a and S21a, respectively. Low alloying of Bi (or In), whereby we purposefully introduce new B′(III) sites (<10% loading), causes new resonances to appear in the ^{133}Cs NMR spectra as well as increases the presence of spinning side bands across all three NMR-active nuclei (^{115}In, ^{133}Cs, and ^{209}Bi) studied here, consistent with an increase in the quadrupole coupling interaction. With the sensitivity of the ^{133}Cs chemical shift

https://dx.doi.org/10.1021/jacs.0c02198
J. Am. Chem. Soc. 2020, 142, 10780−10793

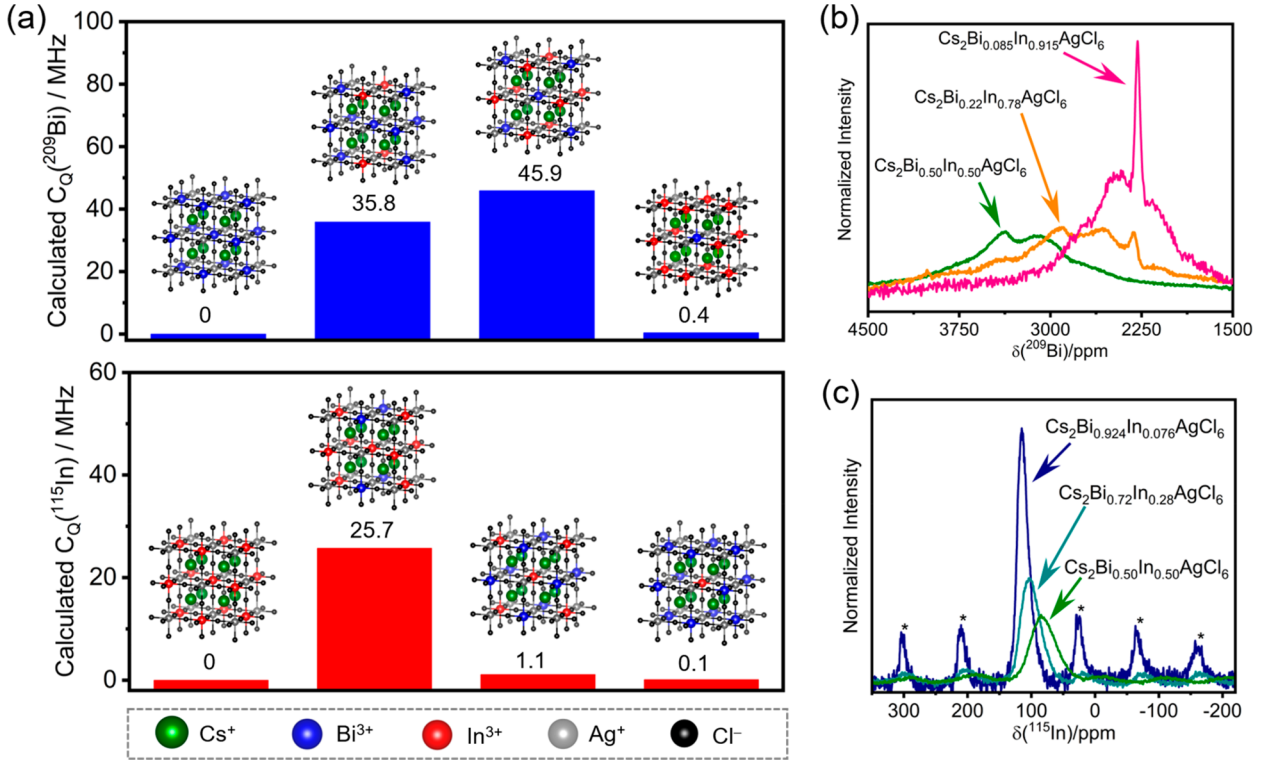

Figure 8. Change in calculated C_Q of the central ^{209}Bi or ^{115}In nuclei with a change in B′(III) site neighbors in the super lattice (a). Normalized ^{209}Bi (b) and ^{115}In (c) NMR spectra acquired at 21.14 T under nonspinning and magic-angle spinning (18 kHz) conditions, respectively, for the samples as indicated. Normalized intensity in b and c corresponds to vertically scaled spectra with the same amount of Bi or In, respectively, for a sample for a given number of scans. Asterisks (*) in c indicate spinning side bands.

and its receptivity, a change in the surrounding eight B″(Ag)/B′(In or Bi) neighbors in the parent materials (i.e., an antisite defect) should induce a new resonance as the alloying discussed above shows. Considering that a spinning side band at <1% intensity is detectable, we predict a new Cs chemical environment induced by an antisite defect would be observed in the parent ^{133}Cs NMR spectra if present at ∼0.15% as each B site substitution would impact eight neighboring Cs sites in the extended unit cell.[71] This is further supported by the very small quadrupole coupling constants for the ^{209}Bi and ^{115}In parent compounds where only a few first-order spinning side bands are observed from the satellite transitions and the PXRD (above), suggesting minimal intrinsic defects in these materials. Taking these factors into consideration, we estimate that intrinsic defects in the parent phases are less than 0.1%. This is in contrast to oxide-based perovskites where antisite defects are commonly observed.[100−102]

Impact of Medium-Range Structure on ^{115}In and ^{209}Bi C_Qs Determined Using Quantum Chemical Calculations. The medium-range structure discussed above was used to describe the appearance of additional ^{115}In and ^{209}Bi NMR resonances upon formation of the various $Cs_2Bi_{1-x}In_xAgCl_6$ solid solutions. As noted, when the extended symmetry begins to break down, the large ^{209}Bi and ^{115}In quadrupole moments result in sizable quadrupole coupling constants for ^{209}Bi and ^{115}In nuclei and their NMR line shapes are then dominated by second-order quadrupolar broadening (i.e., the peaks broaden drastically). For example, previous studies have shown that C_Qs can reach up to 256 ± 10 MHz for ^{209}Bi[93] and 200 ± 4 MHz for ^{115}In;[91] this translates into resonances that span MHz (or 1000s of ppm) at moderate magnetic field strengths.

To assess the range of possible C_Qs when Bi/In substitutions occur, DFT calculations were undertaken on a series of medium-range structural models shown in Figure 8a. The heavy atoms considered in this study as well as the size of the crystal lattice required to properly model the medium-range structure precluded calculation of EFGs for all possible combinations of substitution sites. However, calculations were undertaken with substitutions at a few symmetric positions to provide insight into the possible impact of these substitutions on the EFGs. Calculated ^{209}Bi and ^{115}In C_Q values range from 0 MHz for the $Cs_2BiAgCl_6$ and $Cs_2InAgCl_6$ parent crystal structures to a maximum of 45.9 MHz (^{209}Bi) or 25.7 MHz (^{115}In) for nearly equal Bi/In populations (Figure 8a). The moderately sized quadrupole coupling constants for these symmetrically substituted chemical environments hint that the couplings could increase further when nonsymmetric Bi/In substitutions within the multiple possible environments occur (Figure S20). For example, for $Cs_2Bi_{0.50}In_{0.50}AgCl_6$, only 5 of 12 possible B′(III) substitutions have populations > 10%. If we now consider that each of these substitutions can have multiple arrangements across the first and second B′(III) coordination spheres, a daunting scenario develops where the probability for a particular unique arrangement is considerably less than 10%. Taking these factors into consideration and combining the changes in chemical shifts with the distribution of quadrupole coupling constants yields ^{115}In and ^{209}Bi NMR spectra that are unresolvable. Furthermore, if the C_Q's for any arrangement are larger than those predicted by the symmetrically substituted DFT calculations, it could render the site undetectable (vide

https://dx.doi.org/10.1021/jacs.0c02198
J. Am. Chem. Soc. 2020, 142, 10780−10793

infra) under the experimental conditions used here. We observed a significant loss in both ^{209}Bi and ^{115}In NMR signal intensities upon increments in In or Bi concentrations to form $Cs_2Bi_{1-x}In_xAgCl_6$ solid solutions. Interestingly, further increasing In or Bi concentrations, i.e., toward Bi-doped $Cs_2InAgCl_6$ or In-doped $Cs_2BiAgCl_6$ materials, caused both ^{209}Bi and ^{115}In NMR intensities to increase (Figure 8b and 8c, respectively) due to an increase in medium-range coordination environment. The experimental ^{209}Bi and ^{115}In NMR results for the $Cs_2Bi_{1-x}In_xAgCl_6$ series are shown in Figures S25 and S26, respectively.

Figures S27a and S27b show ^{209}Bi and ^{115}In NMR spectra one may expect for a two-site system, one with C_Q = 0 and with 90% of the NMR sites and the other with C_Q = 45 and 25 MHz, respectively, for ^{209}Bi and ^{115}In (i.e., the maximum values calculated via DFT). Clearly, sites with these magnitudes of C_Q and such a low level of incorporation (i.e., very low doping levels) are beyond the detection limits of current instruments. Note also that these are "best-case" scenarios, in that other factors that may further negatively impact detectability, such as magnetic shielding anisotropy or T_2 relaxation, were not considered in these simulations. Figures S27c and S27d illustrate the impact of C_Q on the intensity of a given NMR site. These demonstrate that one may hope to observe ^{115}In and ^{209}Bi NMR sites impacted by substitution if the probability of that site is a significant percentage of the total. Figures S27e and S27f illustrate overlays of simulated NMR spectra expected for a system with two sites with equal probability, one C_Q = 0 and the other with significant C_Q values. These simulated spectra illustrate that there may very well be undetectable ^{209}Bi and ^{115}In NMR sites in our NMR spectra. These simulations also demonstrate that considering that the NMR sites vary only in the nature of the substitutions at the first or second B′(III) coordination spheres (i.e., >7 Å) they will not vary greatly in isotropic chemical shifts, and thus, we cannot hope to resolve distinct sites even at the high field (21.14 T) used here. As noted above, for most of these systems, one needs to consider a minimum of 12 unique Bi/In positions, and thus, observed NMR sites are probably contributions from multiple distinct sites. As such, we refrain from fitting these data due to the lack of resolution and confidence in observing all Bi (or In) resonances. Wideline approaches[103,104] such as WURST, CPMG, or VOCS, which have been successful to detect broad quadrupolar line shapes, would not provide the resolution that is needed here and thus probably would not help decipher these complex spectra.

CONCLUSIONS

We presented an analysis of a lead-free and environmentally stable $Cs_2Bi_{1-x}In_xAgCl_6$ double perovskite series in which indium composition (x) can be tuned from 0 to 1. The Bi/In alloying allows exquisite tailoring of the band-gap properties with an indirect to direct band-gap crossover occurring at x > 0.5. These HDP materials are capable of broad-band white-light PL emission upon ultraviolet excitation, and the emission efficiency highly depends on Bi/In compositional ratios. The Bi-rich materials with an indirect band gap show lower PLQY as compared to In-rich materials with a direct band gap which has a maximum PLQY of 34 ± 4%. PL spectroscopy reveals white-light production from a unique source for these HDPs with an average PL carrier lifetime of approximately 1 μs.

The PXRD information elucidates comprehensive long-range structural behavior, indicating solid solutions through a Vegard's analysis for these $Cs_2Bi_{1-x}In_xAgCl_6$ HDPs. Building beyond these findings a unique short- and medium-range structural evolution can be uncovered using a combination of solid-state NMR spectroscopy of exotic quadrupolar nuclei. Specifically, we have shown that there is a high degree of B′(III)/B″(I) site ordering; complementary XRD and NMR results reveal complete Bi^{3+}/In^{3+} mixing with no evidence of phase segregation or antisite defects (<0.1%) in these HDPs. Furthermore, a maximum PLQY is observed when Bi is surrounded by 12 In neighbors about its medium-range structure. This work demonstrates the intricate atomic-level chemical structural information afforded by NMR spectroscopy of these newly developed solid-state optoelectronic-based HDP materials, especially when cationic mixing is present.

ASSOCIATED CONTENT

Supporting Information

The Supporting Information is available free of charge at https://pubs.acs.org/doi/10.1021/jacs.0c02198.

Detailed discussion of synthesis, experimental techniques; EDS, ICP-OES, PL, TGA, XRD, NMR and DFT results are located in Tables S1−S6 and Figures S1−S27 (PDF)

AUTHOR INFORMATION

Corresponding Author

Vladimir K. Michaelis − *Department of Chemistry, University of Alberta, Edmonton, Alberta T6G 2G2, Canada;* orcid.org/0000-0002-6708-7660; Email: vladimir.michaelis@ualberta.ca

Authors

Abhoy Karmakar − *Department of Chemistry, University of Alberta, Edmonton, Alberta T6G 2G2, Canada*

Guy M. Bernard − *Department of Chemistry, University of Alberta, Edmonton, Alberta T6G 2G2, Canada*

Alkiviathes Meldrum − *Department of Physics, University of Alberta, Edmonton, Alberta T6G 2E1, Canada;* orcid.org/0000-0001-7215-4023

Anton O. Oliynyk − *Chemistry and Biochemistry Department, Manhattan College, Riverdale, New York 10471, United States;* orcid.org/0000-0003-0732-7340

Complete contact information is available at: https://pubs.acs.org/10.1021/jacs.0c02198

Author Contributions

All authors have given approval to the final version of the manuscript.

Notes

The authors declare no competing financial interest.

ACKNOWLEDGMENTS

The Natural Sciences and Engineering Research Council (NSERC) of Canada, Canada Foundation for Innovation (CFI), Future Energy Systems (CFREF), NSERC CREATE (ATUMS), and University of Alberta are acknowledged for generous research support (V.K.M.). A.K. was supported by an Alberta Innovates Graduate Student Scholarship. Access to the 21.14 T NMR spectrometer was provided by the National Ultrahigh-Field NMR Facility for Solids (Ottawa, Canada), a national research facility funded by a consortium of Canadian Universities and by an NSERC RTI grant, supported by the

National Research Council of Canada and Bruker BioSpin, and managed by the University of Ottawa (www.nmr900.ca). A.O.O. thanks Compute Canada and Kakos Center for Scientific Computing at Manhattan College for providing computational resources. The authors thank Dr. Victor Terskikh and Mr. Amit Bhattacharya for assistance with experiments and scientific discussions.

REFERENCES

(1) National Renewable Energy Laboratory (NREL). *Best Research-Cell Efficiency Chart*. https://www.nrel.gov/pv/assets/pdfs/best-research-cell-efficiencies.20190923.pdf.
(2) Wei, Y.; Cheng, Z.; Lin, J. An Overview on Enhancing the Stability of Lead Halide Perovskite Quantum Dots and Their Applications in Phosphor-Converted LEDs. *Chem. Soc. Rev.* **2019**, *48*, 310−350.
(3) Zhao, Y.; Zhu, K. Organic-Inorganic Hybrid Lead Halide Perovskites for Optoelectronic and Electronic Applications. *Chem. Soc. Rev.* **2016**, *45*, 655−689.
(4) Kovalenko, M. V.; Protesescu, L.; Bodnarchuk, M. I. Properties and Potential Optoelectronic Applications of Lead Halide Perovskite Nanocrystals. *Science* **2017**, *358*, 745−750.
(5) Sutherland, B. R.; Sargent, E. H. Perovskite Photonic Sources. *Nat. Photonics* **2016**, *10*, 295−302.
(6) Luo, J.; Im, J. H.; Mayer, M. T.; Schreier, M.; Nazeeruddin, M. K.; Park, N. G.; Tilley, S. D.; Fan, H. J.; Grätzel, M. Water Photolysis at 12.3% Efficiency via Perovskite Photovoltaics and Earth-Abundant Catalysts. *Science* **2014**, *345*, 1593−1596.
(7) Yakunin, S.; Sytnyk, M.; Kriegner, D.; Shrestha, S.; Richter, M.; Matt, G. J.; Azimi, H.; Brabec, C. J.; Stangl, J.; Kovalenko, M. V.; Heiss, W. Detection of X-Ray Photons by Solution-Processed Lead Halide Perovskites. *Nat. Photonics* **2015**, *9*, 444−449.
(8) LED Lighting, U.S. Department of Energy; https://www.energy.gov/energysaver/save-electricity-and-fuel/lighting-choices-save-you-money/led-lighting (accessed Dec 2019).
(9) Manser, J. S.; Christians, J. A.; Kamat, P. V. Intriguing Optoelectronic Properties of Metal Halide Perovskites. *Chem. Rev.* **2016**, *116*, 12956−13008.
(10) Dohner, E. R.; Hoke, E. T.; Karunadasa, H. I. Self-Assembly of Broadband White-Light Emitters. *J. Am. Chem. Soc.* **2014**, *136*, 1718−1721.
(11) Smith, M. D.; Connor, B. A.; Karunadasa, H. I. Tuning the Luminescence of Layered Halide Perovskites. *Chem. Rev.* **2019**, *119*, 3104−3139.
(12) Smith, M. D.; Karunadasa, H. I. White-Light Emission from Layered Halide Perovskites. *Acc. Chem. Res.* **2018**, *51*, 619−627.
(13) Wang, M.; Guo, G.-C. Inorganic−Organic Hybrid White Light Phosphors. *Chem. Commun.* **2016**, *52*, 13194−13204.
(14) Shang, M.; Li, C.; Lin, J. How to Produce White Light in a Single-Phase Host? *Chem. Soc. Rev.* **2014**, *43*, 1372−1386.
(15) Yang, J.; Siempelkamp, B. D.; Mosconi, E.; De Angelis, F.; Kelly, T. L. Origin of the Thermal Instability in $CH_3NH_3PbI_3$ Thin Films Deposited on ZnO. *Chem. Mater.* **2015**, *27*, 4229−4236.
(16) Askar, A. M.; Bernard, G. M.; Wiltshire, B.; Shankar, K.; Michaelis, V. K. Multinuclear Magnetic Resonance Tracking of Hydro, Thermal, and Hydrothermal Decomposition of $CH_3NH_3PbI_3$. *J. Phys. Chem. C* **2017**, *121*, 1013−1024.
(17) Needleman, H. Lead Poisoning. *Annu. Rev. Med.* **2004**, *55*, 209−222.
(18) Babayigit, A.; Ethirajan, A.; Muller, M.; Conings, B. Toxicity of Organometal Halide Perovskite Solar Cells. *Nat. Mater.* **2016**, *15*, 247−251.
(19) Yang, J.; Siempelkamp, B. D.; Liu, D.; Kelly, T. L. Investigation Of $CH_3NH_3PbI_3$ Degradation Rates and Mechanisms in Controlled Humidity Environments Using In Situ Techniques. *ACS Nano* **2015**, *9*, 1955−1963.
(20) Domanski, K.; Alharbi, E. A.; Hagfeldt, A.; Grätzel, M.; Tress, W. Systematic Investigation of the Impact of Operation Conditions on the Degradation Behaviour of Perovskite Solar Cells. *Nat. Energy* **2018**, *3*, 61−67.
(21) Li, J.; Cao, H.; Jiao, W.; Wang, Q.; Wei, M.; Cantone, I.; Lü, J.; Abate, A. Biological Impact of Lead from Halide Perovskites Reveals the Risk of Introducing a Safe Threshold. *Nat. Commun.* **2020**, *11*, 310.
(22) Abate, A. Perovskite Solar Cells Go Lead Free. *Joule* **2017**, *1*, 659−664.
(23) Shi, Z.; Guo, J.; Chen, Y.; Li, Q.; Pan, Y.; Zhang, H.; Xia, Y.; Huang, W. Lead-Free Organic−Inorganic Hybrid Perovskites for Photovoltaic Applications: Recent Advances and Perspectives. *Adv. Mater.* **2017**, *29*, 1605005.
(24) Luo, J.; Wang, X.; Li, S.; Liu, J.; Guo, Y.; Niu, G.; Yao, L.; Fu, Y.; Gao, L.; Dong, Q.; Zhao, C.; Leng, M.; Ma, F.; Liang, W.; Wang, L.; Jin, S.; Han, J.; Zhang, L.; Etheridge, J.; Wang, J.; Yan, Y.; Sargent, E. H.; Tang, J. Efficient and Stable Emission of Warm-White Light from Lead-Free Halide Double Perovskites. *Nature* **2018**, *563*, 541−545.
(25) Gray, M. B.; Majher, J. D.; Strom, T. A.; Woodward, P. M. Broadband White Emission in $Cs_2AgIn_{1-x}Bi_xCl_6$ Phosphors. *Inorg. Chem.* **2019**, *58*, 13403−13410.
(26) Yang, B.; Mao, X.; Hong, F.; Meng, W.; Tang, Y.; Xia, X.; Yang, S.; Deng, W.; Han, K. Lead-Free Direct Bandgap Double Perovskite Nanocrystals with Bright Dual-Color Emission. *J. Am. Chem. Soc.* **2018**, *140*, 17001−17006.
(27) Majher, J. D.; Gray, M. B.; Strom, T. A.; Woodward, P. M. $Cs_2NaBiCl_6$: Mn^{2+}- A New Orange-Red Halide Double Perovskite Phosphor. *Chem. Mater.* **2019**, *31*, 1738−1744.
(28) Hu, Q.; Niu, G.; Zheng, Z.; Li, S.; Zhang, Y.; Song, H.; Zhai, T.; Tang, J. Tunable Color Temperatures and Efficient White Emission from $Cs_2Ag_{1-x}Na_xIn_{1-y}Bi_yCl_6$ Double Perovskite Nanocrystals. *Small* **2019**, *15*, 1903496.
(29) Locardi, F.; Cirignano, M.; Baranov, D.; Dang, Z.; Prato, M.; Drago, F.; Ferretti, M.; Pinchetti, V.; Fanciulli, M.; Brovelli, S.; De Trizio, L.; Manna, L. Colloidal Synthesis of Double Perovskite $Cs_2AgInCl_6$ and Mn-Doped $Cs_2AgInCl_6$ Nanocrystals. *J. Am. Chem. Soc.* **2018**, *140*, 12989−12995.
(30) Lee, W.; Hong, S.; Kim, S. Colloidal Synthesis of Lead-Free Silver−Indium Double-Perovskite $Cs_2AgInCl_6$ Nanocrystals and Their Doping with Lanthanide Ions. *J. Phys. Chem. C* **2019**, *123*, 2665−2672.
(31) Zhou, J.; Rong, X.; Zhang, P.; Molokeev, M. S.; Wei, P.; Liu, Q. Manipulation of Bi^{3+}/In^{3+} Transmutation and Mn^{2+} -Doping Effect on the Structure and Optical Properties of Double Perovskite $Cs_2NaBi_{1-x}In_xCl_6$. *Adv. Opt. Mater.* **2019**, *1801435*, 1−9.
(32) Luo, J.; Hu, M.; Niu, G.; Tang, J. Lead-Free Halide Perovskites and Perovskite Variants as Phosphors toward Light-Emitting Applications. *ACS Appl. Mater. Interfaces* **2019**, *11*, 31575−31584.
(33) Lamba, R. S.; Basera, P.; Bhattacharya, S.; Sapra, S. Band Gap Engineering in $Cs_2(Na_xAg_{1-x})BiCl_6$ Double Perovskite Nanocrystals. *J. Phys. Chem. Lett.* **2019**, *10*, 5173−5181.
(34) Liu, Y.; Jing, Y.; Zhao, J.; Liu, Q.; Xia, Z. Design Optimization of Lead-Free Perovskite $Cs_2AgInCl_6$:Bi Nanocrystals with 11.4% Photoluminescence Quantum Yield. *Chem. Mater.* **2019**, *31*, 3333−3339.
(35) Slavney, A. H.; Hu, T.; Lindenberg, A. M.; Karunadasa, H. I. A Bismuth-Halide Double Perovskite with Long Carrier Recombination Lifetime for Photovoltaic Applications. *J. Am. Chem. Soc.* **2016**, *138*, 2138−2141.
(36) McClure, E. T.; Ball, M. R.; Windl, W.; Woodward, P. M. Cs_2AgBiX_6 (X = Br, Cl): New Visible Light Absorbing, Lead-Free Halide Perovskite Semiconductors. *Chem. Mater.* **2016**, *28*, 1348−1354.
(37) Volonakis, G.; Filip, M. R.; Haghighirad, A. A.; Sakai, N.; Wenger, B.; Snaith, H. J.; Giustino, F. Lead-Free Halide Double Perovskites via Heterovalent Substitution of Noble Metals. *J. Phys. Chem. Lett.* **2016**, *7*, 1254−1259.
(38) Filip, M. R.; Liu, X.; Miglio, A.; Hautier, G.; Giustino, F. Phase Diagrams and Stability of Lead-Free Halide Double Perovskites

https://dx.doi.org/10.1021/jacs.0c02198
J. Am. Chem. Soc. 2020, 142, 10780−10793

$Cs_2BB'X_6$: B = Sb and Bi, B′ = Cu, Ag, and Au, and X = Cl, Br, and I. *J. Phys. Chem. C* **2018**, *122*, 158−170.
(39) K, N. N.; Nag, A. Synthesis and Luminescence of Mn-Doped $Cs_2AgInCl_6$ Double Perovskites. *Chem. Commun.* **2018**, *54*, 5205−5208.
(40) Lawson, K. E. Optical Studies of Electronic Transitions in Hexa- and Tetracoordinated Mn^{2+} Crystals. *J. Chem. Phys.* **1967**, *47*, 3627−3633.
(41) Zeng, R.; Zhang, L.; Xue, Y.; Ke, B.; Zhao, Z.; Huang, D.; Wei, Q.; Zhou, W.; Zou, B. Highly Efficient Blue Emission from Self-Trapped Excitons in Stable Sb^{3+}-Doped $Cs_2NaInCl_6$ Double Perovskites. *J. Phys. Chem. Lett.* **2020**, *11*, 2053−2061.
(42) Locardi, F.; Sartori, E.; Buha, J.; Zito, J.; Prato, M.; Pinchetti, V.; Zaffalon, M. L.; Ferretti, M.; Brovelli, S.; Infante, I.; De Trizio, L.; Manna, L. Emissive Bi-Doped Double Perovskite $Cs_2Ag_{1-x}Na_xInCl_6$ Nanocrystals. *ACS Energy Lett.* **2019**, *4*, 1976−1982.
(43) Hu, Z.; Lin, Z.; Su, J.; Zhang, J.; Chang, J.; Hao, Y. A Review on Energy Band-Gap Engineering for Perovskite Photovoltaics. *Sol. RRL* **2019**, *3*, 1900304.
(44) Xiao, Z.; Zhou, Y.; Hosono, H.; Kamiya, T.; Padture, N. P. Bandgap Optimization of Perovskite Semiconductors for Photovoltaic Applications. *Chem. - Eur. J.* **2018**, *24*, 2305−2316.
(45) Du, K. Z.; Meng, W.; Wang, X.; Yan, Y.; Mitzi, D. B. Bandgap Engineering of Lead-Free Double Perovskite $Cs_2AgBiBr_6$ through Trivalent Metal Alloying. *Angew. Chem., Int. Ed.* **2017**, *56*, 8158−8162.
(46) Gray, M. B.; McClure, E. T.; Woodward, P. M. $Cs_2AgBiBr_{6-x}Cl_x$ Solid Solutions-Band Gap Engineering with Halide Double Perovskites. *J. Mater. Chem. C* **2019**, *7*, 9686−9689.
(47) Jiang, J. T.; Xiu, S. L.; Zheng, M. M.; Jia, T. T.; Liu, H. Y.; Zhang, Y.; Chen, G. Indirect−Direct Bandgap Transition and Gap Width Tuning in Bilayer MoS_2 Superlattices. *Chem. Phys. Lett.* **2014**, *613*, 74−79.
(48) Wang, Y. J.; Zhou, K. G.; Yu, G.; Zhong, X.; Zhang, H. L. Partial Oxidized Arsenene: Emerging Tunable Direct Bandgap Semiconductor. *Sci. Rep.* **2016**, *6*, 24981.
(49) Chen, X.; Yang, Q.; Meng, R.; Jiang, J.; Liang, Q.; Tan, C.; Sun, X. The Electronic and Optical Properties of Novel Germanene and Antimonene Heterostructures. *J. Mater. Chem. C* **2016**, *4*, 5434−5441.
(50) Tran, T. T.; Panella, J. R.; Chamorro, J. R.; Morey, J. R.; McQueen, T. M. Designing Indirect-Direct Bandgap Transitions in Double Perovskites. *Mater. Horiz.* **2017**, *4*, 688−693.
(51) Volonakis, G.; Haghighirad, A. A.; Milot, R. L.; Sio, W. H.; Filip, M. R.; Wenger, B.; Johnston, M. B.; Herz, L. M.; Snaith, H. J.; Giustino, F. $Cs_2InAgCl_6$: A New Lead-Free Halide Double Perovskite with Direct Band Gap. *J. Phys. Chem. Lett.* **2017**, *8*, 772−778.
(52) Askar, A. M.; Karmakar, A.; Bernard, G. M.; Ha, M.; Terskikh, V. V.; Wiltshire, B. D.; Patel, S.; Fleet, J.; Shankar, K.; Michaelis, V. K. Composition-Tunable Formamidinium Lead Mixed Halide Perovskites via Solvent-Free Mechanochemical Synthesis: Decoding the Pb Environments Using Solid-State NMR Spectroscopy. *J. Phys. Chem. Lett.* **2018**, *9*, 2671−2677.
(53) Pan, C.; Lee, Y. J.; Ammundsen, B.; Grey, C. P. ^{6}Li MAS NMR Studies of the Local Structure and Electrochemical Properties of Cr-Doped Lithium Manganese and Lithium Cobalt Oxide Cathode Materials for Lithium-Ion Batteries. *Chem. Mater.* **2002**, *14*, 2289−2299.
(54) Wasylishen, R. E.; Knop, O.; Macdonald, J. B. Cation Rotation in Methylammonium Lead Halides. *Solid State Commun.* **1985**, *56*, 581−582.
(55) Senocrate, A.; Moudrakovski, I.; Kim, G. Y.; Yang, T.; Gregori, G.; Grätzel, M.; Maier, J. The Nature of Ion Conduction in Methylammonium Lead Iodide: A Multimethod Approach. *Angew. Chem., Int. Ed.* **2017**, *56*, 7755−7759.
(56) Senocrate, A.; Moudrakovski, I.; Maier, J. Short-Range Ion Dynamics in Methylammonium Lead Iodide by Multinuclear Solid State NMR and ^{127}I NQR. *Phys. Chem. Chem. Phys.* **2018**, *20*, 20043−20055.
(57) Kubicki, D. J.; Prochowicz, D.; Hofstetter, A.; Péchy, P.; Zakeeruddin, S. M.; Grätzel, M.; Emsley, L. Cation Dynamics in Mixed-Cation $(MA)_x(FA)_{1-x}PbI_3$ Hybrid Perovskites from Solid-State NMR. *J. Am. Chem. Soc.* **2017**, *139*, 10055−10061.
(58) Kubicki, D. J.; Prochowicz, D.; Hofstetter, A.; Saski, M.; Yadav, P.; Bi, D.; Pellet, N.; Lewiński, J.; Zakeeruddin, S. M.; Grätzel, M.; Emsley, L. Formation of Stable Mixed Guanidinium-Methylammonium Phases with Exceptionally Long Carrier Lifetimes for High-Efficiency Lead Iodide-Based Perovskite Photovoltaics. *J. Am. Chem. Soc.* **2018**, *140*, 3345−3351.
(59) Hanrahan, M. P.; Men, L.; Rosales, B. A.; Vela, J.; Rossini, A. J. Sensitivity-Enhanced ^{207}Pb Solid-State NMR Spectroscopy for the Rapid, Non-Destructive Characterization of Organolead Halide Perovskites. *Chem. Mater.* **2018**, *30*, 7005−7015.
(60) Kubicki, D. J.; Prochowicz, D.; Pinon, A.; Stevanato, G.; Hofstetter, A.; Zakeeruddin, S. M.; Grätzel, M.; Emsley, L. Doping and Phase Segregation in Mn^{2+} - and Co^{2+} -Doped Lead Halide Perovskites from ^{133}Cs and ^{1}H NMR Relaxation Enhancement. *J. Mater. Chem. A* **2019**, *7*, 2326−2333.
(61) Franssen, W. M. J.; Kentgens, A. P. M. Solid−State NMR of Hybrid Halide Perovskites. *Solid State Nucl. Magn. Reson.* **2019**, *100*, 36−44.
(62) Franssen, W. M. J.; Van Es, S. G. D.; Dervişoğlu, R.; De Wijs, G. A.; Kentgens, A. P. M. Symmetry, Dynamics, and Defects in Methylammonium Lead Halide Perovskites. *J. Phys. Chem. Lett.* **2017**, *8*, 61−66.
(63) Karmakar, A.; Dodd, M. S.; Zhang, X.; Oakley, M. S.; Klobukowski, M.; Michaelis, V. K. Mechanochemical Synthesis of 0D and 3D Cesium Lead Mixed Halide Perovskites. *Chem. Commun.* **2019**, *55*, 5079−5082.
(64) Chen, Y.; Smock, S. R.; Flintgruber, A. H.; Perras, F. A.; Brutchey, R. L.; Rossini, A. J. Surface Termination of $CsPbBr_3$ Perovskite Quantum Dots Determined by Solid-State NMR Spectroscopy. *J. Am. Chem. Soc.* **2020**, *142*, 6117−6127.
(65) Kubicki, D. J.; Prochowicz, D.; Salager, E.; Rakhmatullin, A.; Grey, C. P.; Emsley, L.; Stranks, S. D. Local Structure and Dynamics in Methylammonium, Formamidinium and Cesium Tin(II) Mixed−halide Perovskites from ^{119}Sn Solid-State NMR. *J. Am. Chem. Soc.* **2020**, *142*, 7813−7826.
(66) Karmakar, A.; Askar, A. M.; Bernard, G. M.; Terskikh, V. V.; Ha, M.; Patel, S.; Shankar, K.; Michaelis, V. K. Mechanochemical Synthesis of Methylammonium Lead Mixed-Halide Perovskites: Unraveling the Solid-Solution Behavior Using Solid-State NMR. *Chem. Mater.* **2018**, *30*, 2309−2321.
(67) Rosales, B. A.; Men, L.; Cady, S. D.; Hanrahan, M. P.; Rossini, A. J.; Vela, J. Persistent Dopants and Phase Segregation in Organolead Mixed-Halide Perovskites. *Chem. Mater.* **2016**, *28*, 6848−6859.
(68) Kubicki, D. J.; Prochowicz, D.; Hofstetter, A.; Zakeeruddin, S. M.; Grätzel, M.; Emsley, L. Phase Segregation in Potassium-Doped Lead Halide Perovskites from ^{39}K Solid-State NMR at 21.1 T. *J. Am. Chem. Soc.* **2018**, *140*, 7232−7238.
(69) Kubicki, D. J.; Prochowicz, D.; Hofstetter, A.; Zakeeruddin, S. M.; Grätzel, M.; Emsley, L. Phase Segregation in Cs-, Rb- and K-Doped Mixed-Cation $(MA)_x(FA)_{1-x}PbI_3$ Hybrid Perovskites from Solid-State NMR. *J. Am. Chem. Soc.* **2017**, *139*, 14173−14180.
(70) Karmakar, A.; Dodd, M. S.; Agnihotri, S.; Ravera, E.; Michaelis, V. K. Cu(II)-Doped $Cs_2SbAgCl_6$ Double Perovskite: A Lead-Free, Low-Bandgap Material. *Chem. Mater.* **2018**, *30*, 8280−8290.
(71) Michaelis, V. K.; Greer, B. J.; Aharen, T.; Greedan, J. E.; Kroeker, S. Determining Electron Spin-Transfer Mechanisms in Paramagnetic Ba_2YMO_6 (M = Mo, Re, Ru) Double Perovskites by ^{89}Y and ^{137}Ba MAS NMR Spectroscopy. *J. Phys. Chem. C* **2012**, *116*, 23646−23652.
(72) Aharen, T.; Greedan, J. E.; Bridges, C. A.; Aczel, A. A.; Rodriguez, J.; Macdougall, G.; Luke, G. M.; Imai, T.; Michaelis, V. K.; Kroeker, S.; Zhou, H.; Wiebe, C. R.; Cranswick, L. M. D. Magnetic Properties of the Geometrically Frustrated S = 1/2 Antiferromagnets, La_2LiMoO_6 and Ba_2YMoO_6, with the B-Site Ordered Double

https://dx.doi.org/10.1021/jacs.0c02198
J. Am. Chem. Soc. 2020, 142, 10780−10793

Perovskite Structure: Evidence for a Collective Spin-Singlet Ground State. *Phys. Rev. B: Condens. Matter Mater. Phys.* **2010**, *81*, 224409.
(73) Li, T.; Zhao, X.; Yang, D.; Du, M. H.; Zhang, L. Intrinsic Defect Properties in Halide Double Perovskites for Optoelectronic Applications. *Phys. Rev. Appl.* **2018**, *10*, 041001.
(74) Goldschmidt, V. M. Die Gesetze Der Krystallochemie. *Naturwissenschaften* **1926**, *14*, 477−485.
(75) Li, C.; Lu, X.; Ding, W.; Feng, L.; Gao, Y.; Guo, Z. Formability of ABX_3 (X = F, Cl, Br, I) Halide Perovskites. *Acta Crystallogr., Sect. B: Struct. Sci.* **2008**, *B64*, 702−707.
(76) Shannon, R. D. Revised Effective Ionic Radii and Systematic Studies of Interatomie Distances in Halides and Chaleogenides. *Acta Crystallogr., Sect. A: Cryst. Phys., Diffr., Theor. Gen. Crystallogr.* **1976**, *A32*, 751−767.
(77) Kubelka, P.; Munk, F. Ein Beitrag Zur Optik Der Farbanstriche. *Z.Technol. Phys. (Leipzig)* **1931**, *12*, 593−601.
(78) Slavney, A. H.; Leppert, L.; Bartesaghi, D.; Gold-Parker, A.; Toney, M. F.; Savenije, T. J.; Neaton, J. B.; Karunadasa, H. I. Defect-Induced Band-Edge Reconstruction of a Bismuth-Halide Double Perovskite for Visible-Light Absorption. *J. Am. Chem. Soc.* **2017**, *139* (14), 5015−5018.
(79) Meng, W.; Wang, X.; Xiao, Z.; Wang, J.; Mitzi, D. B.; Yan, Y. Parity-Forbidden Transitions and Their Impact on the Optical Absorption Properties of Lead-Free Metal Halide Perovskites and Double Perovskites. *J. Phys. Chem. Lett.* **2017**, *8*, 2999−3007.
(80) Steele, J. A.; Puech, P.; Keshavarz, M.; Yang, R.; Banerjee, S.; Debroye, E.; Kim, C. W.; Yuan, H.; Heo, N. H.; Vanacken, J.; Walsh, A.; Hofkens, J.; Roeffaers, M. B. J. Giant Electron−Phonon Coupling and Deep Conduction Band Resonance in Metal Halide Double Perovskite. *ACS Nano* **2018**, *12*, 8081−8090.
(81) Jakob, M.; Aissiou, A.; Morrish, W.; Marsiglio, F.; Islam, M.; Kartouzian, A.; Meldrum, A. Reappraising the Luminescence Lifetime Distributions in Silicon Nanocrystals. *Nanoscale Res. Lett.* **2018**, *13*, 383.
(82) Thirumal, K.; Chong, W. K.; Xie, W.; Ganguly, R.; Muduli, S. K.; Sherburne, M.; Asta, M.; Mhaisalkar, S.; Sum, T. C.; Soo, H. S.; Mathews, N. Morphology-Independent Stable White-Light Emission from Self-Assembled Two-Dimensional Perovskites Driven by Strong Exciton-Phonon Coupling to the Organic Framework. *Chem. Mater.* **2017**, *29*, 3947−3953.
(83) Luo, J.; Li, S.; Wu, H.; Zhou, Y.; Li, Y.; Liu, J.; Li, J.; Li, K.; Yi, F.; Niu, G.; Tang, J. $Cs_2AgInCl_6$ Double Perovskite Single Crystals: Parity Forbidden Transitions and Their Application for Sensitive and Fast UV Photodetectors. *ACS Photonics* **2018**, *5*, 398−405.
(84) Johnston, M. B.; Herz, L. M. Hybrid Perovskites for Photovoltaics: Charge-Carrier Recombination, Diffusion, and Radiative Efficiencies. *Acc. Chem. Res.* **2016**, *49*, 146−154.
(85) Dequilettes, D. W.; Frohna, K.; Emin, D.; Kirchartz, T.; Bulovic, V.; Ginger, D. S.; Stranks, S. D. Charge-Carrier Recombination in Halide Perovskites. *Chem. Rev.* **2019**, *119*, 11007−11019.
(86) Vegard, L. Die Konstitution Der Mischkristalle Und Die Raumffillung Der Atome. *Eur. Phys. J. A* **1921**, *5*, 17−26.
(87) Harris, R. K.; Becker, E. D.; Cabral de Menezes, S. M.; Goodfellow, R.; Granger, P. NMR Nomenclature. Nuclear Spin Properties and Conventions for Chemical Shifts. *Pure Appl. Chem.* **2001**, *73*, 1795−1818.
(88) Michaelis, V. K.; Aguiar, P. M.; Kroeker, S. Probing Alkali Coordination Environments in Alkali Borate Glasses by Multinuclear Magnetic Resonance. *J. Non-Cryst. Solids* **2007**, *353*, 2582−2590.
(89) Kroeker, S.; Eichele, K.; Wasylishen, R. E.; Britten, J. F. Cesium-133 NMR Study of $CsCd(SCN)_3$: Relative Orientation of the Chemical Shift and Electric Field Gradient Tensors. *J. Phys. Chem. B* **1997**, *101*, 3727−3733.
(90) MacKenzie, K. J.; Smith, M. E. *Multinuclear Solid-State Nuclear Magnetic Resonance of Inorganic Materials*; Elsevier, 2002.
(91) Chen, F.; Ma, G.; Cavell, R. G.; Terskikh, V.; Wasylishen, R. E. Solid-State ^{115}In NMR Study of Indium Coordination Complexes. *Chem. Commun.* **2008**, 5933−5935.
(92) Chen, F.; Ma, G.; Bernard, G. M.; Cavell, R. G.; Mcdonald, R.; Ferguson, M. J.; Wasylishen, R. E. Solid-State ^{115}In and ^{31}P NMR Studies of Triarylphosphine Indium Trihalide Adducts. *J. Am. Chem. Soc.* **2010**, *132*, 5479−5493.
(93) Hamaed, H.; Laschuk, M. W.; Terskikh, V. V.; Schurko, R. W. Application of Solid-State ^{209}Bi NMR to the Structural Characterization of Bismuth-Containing Materials. *J. Am. Chem. Soc.* **2009**, *131*, 8271−8279.
(94) Bernard, G. M.; Wasylishen, R. E.; Ratcliffe, C. I.; Terskikh, V.; Wu, Q.; Buriak, J. M.; Hauger, T. Methylammonium Cation Dynamics in Methylammonium Lead Halide Perovskites: A Solid-State NMR Perspective. *J. Phys. Chem. A* **2018**, *122*, 1560−1573.
(95) Taylor, R. E.; Beckmann, P. A.; Bai, S.; Dybowski, C. ^{127}I and ^{207}Pb Solid-State NMR Spectroscopy and Nuclear Spin Relaxation in PbI_2: A Preliminary Study. *J. Phys. Chem. C* **2014**, *118*, 9143−9153.
(96) Greer, B. J.; Michaelis, V. K.; Terskikh, V. V.; Kroeker, S. Reconnaissance of Diverse Structural and Electronic Environments in Germanium Halides by Solid-State ^{73}Ge NMR and Quantum Chemical Calculations. *Can. J. Chem.* **2011**, *89*, 1118−1129.
(97) Hamaed, H.; Johnston, K. E.; Cooper, B. F. T.; Terskikh, V. V.; Ye, E.; Macdonald, C. L. B.; Arnold, D. C.; Schurko, R. W. A ^{115}In Solid-State NMR Study of Low Oxidation-State Indium Complexes. *Chem. Sci.* **2014**, *5*, 982−995.
(98) Lan, C.; Zhao, S.; Luo, J.; Fan, P. First-Principles Study of Anion Diffusion in Lead-Free Halide Double Perovskites. *Phys. Chem. Chem. Phys.* **2018**, *20*, 24339−24344.
(99) Zhao, X. G.; Yang, J. H.; Fu, Y.; Yang, D.; Xu, Q.; Yu, L.; Wei, S. H.; Zhang, L. Design of Lead-Free Inorganic Halide Perovskites for Solar Cells via Cation-Transmutation. *J. Am. Chem. Soc.* **2017**, *139*, 2630−2638.
(100) Muñoz-García, A. B.; Pavone, M.; Carter, E. A. Effect of Antisite Defects on the Formation of Oxygen Vacancies in Sr_2FeMoO_6: Implications for Ion and Electron Transport. *Chem. Mater.* **2011**, *23*, 4525−4536.
(101) Colis, S.; Stoeffler, D.; Meny, C.; Fix, T.; Leuvrey, C.; Pourroy, G.; Dinia, A.; Panissod, P. Structural Defects in Sr_2FeMoO_6 Double Perovskite: Experimental versus Theoretical Approach. *J. Appl. Phys.* **2005**, *98*, 033905.
(102) Greneche, J. M.; Venkatesan, M.; Suryanarayanan, R.; Coey, J. M. D. Mössbauer Spectrometry of A_2FeMoO_6 (A = Ca, Sr, Ba): Search for Antiphase Domains. *Phys. Rev. B: Condens. Matter Mater. Phys.* **2001**, *63*, 174403.
(103) O'Dell, L. A. Ultra-Wideline Solid-State NMR: Developments and Applications of the WCPMG Experiment. In *Modern Magnetic Resonance*; Webb, G., Eds.; Springer: Cham, 2017.
(104) O'Dell, L. A.; Schurko, R. W. QCPMG Using Adiabatic Pulses for Faster Acquisition of Ultra-Wideline NMR Spectra. *Chem. Phys. Lett.* **2008**, *464*, 97−102.

https://dx.doi.org/10.1021/jacs.0c02198
J. Am. Chem. Soc. 2020, 142, 10780−10793